



**HAL**  
open science

## Three-dimensional shear velocity structure of the Mauleon and Arzacq basins (Western Pyrenees)

Maximilien Lehujeur, Sébastien Chevrot, Antonio Villaseñor, Emmanuel Masini, Nicolas Saspiturry, Rodolphe Lescoutre, Matthieu Sylvander & The Maupasacq Working Group

► **To cite this version:**

Maximilien Lehujeur, Sébastien Chevrot, Antonio Villaseñor, Emmanuel Masini, Nicolas Saspiturry, et al.. Three-dimensional shear velocity structure of the Mauleon and Arzacq basins (Western Pyrenees). Bulletin de la Société Géologique de France, 2021, 10.1051/bsgf/2021039 . hal-03374923

**HAL Id: hal-03374923**

**<https://hal.science/hal-03374923v1>**

Submitted on 12 Oct 2021

**HAL** is a multi-disciplinary open access archive for the deposit and dissemination of scientific research documents, whether they are published or not. The documents may come from teaching and research institutions in France or abroad, or from public or private research centers.

L'archive ouverte pluridisciplinaire **HAL**, est destinée au dépôt et à la diffusion de documents scientifiques de niveau recherche, publiés ou non, émanant des établissements d'enseignement et de recherche français ou étrangers, des laboratoires publics ou privés.

# 1 **Three-dimensional shear velocity structure of the Mauléon** 2 **and Arzacq basins (Western Pyrenees)**

3 M. Lehujeur<sup>1,2</sup>, S. Chevrot<sup>1</sup>, A. Villaseñor<sup>3</sup>, E. Masini<sup>4,5</sup>, N. Saspiturry<sup>6</sup>,

4 R. Lescoutre<sup>7</sup>, M. Sylvander<sup>8</sup> & the Maupasacq Working Group<sup>9</sup>

<sup>1</sup>*GET, UMR 5563, Observatoire Midi Pyrénées, Université Paul Sabatier, CNRS, IRD, Toulouse, France*

<sup>2</sup>*Université Gustave Eiffel, Allée des Ponts et Chaussées,*

*Route de Bouaye - CS 5004 - 44344 Bouguenais Cedex, France*

<sup>3</sup>*Barcelona Center for Subsurface Imaging, Institute of Marine Sciences, ICM-CSIC, 08003 Barcelona, Spain*

<sup>4</sup>*M&U sas, 3 rue des Abattoirs, 38120 Saint-Egreve, France*

<sup>5</sup>*ISTerre, Université de Grenoble, CS 40700, 38058 Grenoble Cedex 9, France*

<sup>6</sup>*Université Bordeaux Montaigne EA 4592 Géoressources et Environnement,*

*1 allée Fernand Daguin 33607 Pessac cedex, France*

<sup>7</sup>*Uppsala University, Department of Earth Sciences, Villavägen 16, 752 36, Uppsala, Sweden*

<sup>8</sup>*IRAP, UMR 5277, Observatoire Midi Pyrénées, Université Paul Sabatier, CNRS, Toulouse, France.*

5

6 <sup>9</sup> *The Maupasacq working group includes the authors and Magali Collin (Total), Sylvain Calas-*  
7 *sou (Total), Marc Martin (Total), Adnand Bitri (BRGM), Martin Rolland (CNRS), Laurent Stehly (IS-*  
8 *Terre), Jacques Brives (ISTerre), Pierre Boué (ISTerre), Philippe L'Excellent (CNRS), Nikos Mar-*  
9 *takis (Seismotech), Jordi Diaz (CSIC), Stephen Beller (OMP), Frank Grimaud (OMP), Katerina Poly-*  
10 *chronopoulou (Seismotech), Maik Neukirch (CSIC), Juvenal Andres Cabrera (CSIC), Georgios Chris-*  
11 *taras (Seismotech), Ayman Morouj (Seismotech), Boris Boin (CNRS), Sebastien Benhamed (OMP),*  
12 *Paula Romero Lopez (CSIC), Christoforos Toumazatos (Seismotech), Konstantinos Fragiadakis (Seis-*  
13 *motech), Laurie Chopard (CNRS) and Julie Clemente (CNRS).*

14 **SUMMARY**

15  
16 We present a 3-D shear wave velocity model of the Mauléon and Arzacq basins from the  
17 surface down to 10 km depth, inverted from phase velocity maps at periods between 2  
18 and 9 s. These phase velocity maps were obtained by analyzing coherent surface wave  
19 fronts extracted from ambient seismic noise recorded by the large-N Maupasacq seismic  
20 array with a matched filtering approach. This new model is in good agreement with a lo-  
21 cal earthquake tomography study performed on the same acquisition dataset. Our passive  
22 imaging models reveal the upper crustal architecture of the Mauléon and Arzacq basins,  
23 with new details on the basement and its relationship with the overlying sedimentary  
24 cover. Combining these new tomographic images with surface and subsurface geological  
25 information allows us to trace major orogenic structures from the surface down to the  
26 basement. In the basin, the models image the first-order basin architecture with a kilo-  
27 metric resolution. At depth, high velocity anomalies suggest the presence of dense deep  
28 crustal and mantle rocks in the hanging wall of north-vergent Pyrenean thrusts. These  
29 high velocity anomalies spatially coincide with a positive gravity anomaly in the Western  
30 Mauléon basin. In addition, our models reveal major changes from the Chainons Béarnais  
31 to the Western Mauléon basin across a set of orogen-perpendicular structures, the Saison  
32 and the Barlanès transfer zones. These changes reflect the along-strike variation of the  
33 orogenic evolution that led to the preservation of the former rifted domain and its under-  
34 lying mantle in the orogenic wedge of the Western Pyrenees. We discuss the implications  
35 of these results for the 3-D architecture of the Mauléon basin and its underlying basement.

36 *Nous présentons un modèle 3-D de vitesse des ondes de cisaillement des bassins de*  
37 *Mauléon et d'Arzacq de la surface jusqu'à 10 km de profondeur inversé à partir de cartes*  
38 *de vitesse de phase pour des périodes entre 2 et 9 s. Ces cartes ont été obtenues à partir*  
39 *de l'analyse de fronts d'onde de surface cohérents extraits du bruit sismique ambiant en-*  
40 *registré par le réseau Maupasacq par filtrage adaptatif. Ce nouveau modèle est en bon*  
41 *accord avec la tomographie locale réalisée sur ce même jeu de données. Nos nouvelles*  
42 *images tomographiques révèlent l'architecture supra-crustale des bassins de Mauléon*

43 *et d'Arzacq, avec des informations nouvelles sur la nature du socle et sa relation à la*  
44 *couverture sédimentaire. En combinant ces nouvelles images tomographiques aux infor-*  
45 *mations géologiques, il est possible de tracer les principales structures orogéniques de la*  
46 *surface jusqu'au socle des bassins. Dans le bassin, les modèles nous fournissent une im-*  
47 *age de premier ordre des plis et chevauchements à l'échelle kilométrique. En profondeur,*  
48 *les anomalies rapides suggèrent la présence de roches de la croûte inférieure et du man-*  
49 *teau dans le toit des chevauchements pyrénéens de pendage nord. Ces anomalies rapides*  
50 *coïncident spatialement avec l'anomalie gravimétrique positive dans la partie ouest du*  
51 *bassin de Mauléon. Nos modèles tomographiques documentent également des change-*  
52 *ments de structures majeurs entre les Chaînon Béarnais et la partie ouest du bassin de*  
53 *Mauléon à travers des structures perpendiculaires à l'axe de la chaîne, représentées par*  
54 *les structures transverses du Saison et du Barlanès. Ce changement structural reflète les*  
55 *variations latérales de l'évolution orogénique qui a conduit à la préservation des do-*  
56 *maines de rift hyper-étirés et du manteau sous-jacent dans le prisme orogénique. Nous*  
57 *discutons les implications de ces résultats concernant l'architecture 3-D du bassin de*  
58 *Mauléon et du socle sous-jacent.*

59 **Key words:** Pyrenees, Seismic Tomography, Sedimentary Basins, 3-D architecture

## 60 1 INTRODUCTION

61 Imaging crustal structures with a fine spatial resolution is an important goal of modern seismology,  
62 with major implications in domains such as georesources and seismic hazard. In regions where strong  
63 crustal heterogeneity prevails, such as in orogens, passive imaging using local earthquakes remains  
64 challenging owing to the uneven distribution of seismicity, both in time and space, and to the sparsity  
65 of permanent seismic networks. With ambient seismic noise, seismologists can now reconstruct sur-  
66 face waves from pairs of seismic stations, thereby freeing themselves from relying on the occurrence  
67 of natural earthquakes (e.g. Shapiro et al. 2005). Ambient noise surface wave tomography (SWT) has  
68 gained a large interest in the academic world and have been applied to a very broad range of scales  
69 and contexts. Most studies focused on large scale applications like North America (e.g. Lin et al.  
70 2008) or Europe (e.g. Lu et al. 2018). The extension of the method at a regional scale using lower  
71 periods (below 10 s) are often very efficient to image the contours of the sedimentary basins, usually

72 characterized by lower velocities (e.g. Macquet et al. 2014). Fewer studies have focused on the use  
73 of surface waves from the ambient seismic noise to image structures inside a sedimentary basin (Jia  
74 & Clayton (2021) being a recent exception). The advantages related to this passive source of seismic  
75 waves, i.e. continuity of sources and reduced acquisition costs compared to active seismic methods,  
76 did however motivate focused applications on sedimentary basins for example for the characterization  
77 of an oil and gas field (e.g. Mordret et al. 2013), the subsurface imaging for the exploration of deep  
78 geothermal resources (e.g. Lehuteur et al. 2018; Planès et al. 2019) or the monitoring of CO<sub>2</sub> under-  
79 ground storage sites (e.g. Gassenmeier et al. 2014). Another recent advance came from the recognition  
80 that large-N node deployments such as those commonly used in controlled-source acquisitions for the  
81 oil and gas industry provide rich and valuable datasets for passive imaging studies (e.g. Schmandt &  
82 Clayton 2013). These two recent developments have opened important new perspectives not only for  
83 crustal-scale tomography, but also to get valuable insights on the 3-D geometry of sedimentary basins  
84 in structurally complex areas to complement active seismic reflection surveys.

85 To investigate the potential of passive imaging for the characterization of sedimentary basins,  
86 which has so far received little attention from the academic world, we have deployed a large-N array  
87 of 442 sensors, the Maupasacq experiment, in the western part of the northern Pyrenees foothills, from  
88 March to September 2017. The inner part of the network formed a regular  $50 \times 30$  km rectangular  
89 grid, extended to about  $120 \times 130$  km thanks to two additional circular deployments (Fig. 1). In the  
90 inner rectangular grid, the station spacing ranged from 1 km between the geophone nodes to 7 km  
91 between the broad-band stations (details in Polychronopoulou et al. 2018; Lehuteur & Chevrot 2020).  
92 The acquisition covers the Mauléon and Arzacq basins with 191 geophone nodes, 197 short period  
93 instruments, and 54 broadband stations. Despite being widely covered by seismic reflection profiles  
94 and wells thanks to decades of oil and gas exploration, the 3-D architecture of the Mauléon-Arzacq  
95 rift system remains poorly constrained.

96 Different rift phases are regionally recognized during the Mesozoic, but it is well accepted that the  
97 north Pyrenean rift basins are mostly shaped by the Aptian-Cenomanian hyper-extension rifting stage  
98 before being shortened by the Pyrenean orogenesis from Late Cretaceous onwards. The structural  
99 complexity resulting from this polyphasic deformation history probably explains why active deep  
100 reflection seismic techniques failed to image even the first-order geometry of the basins (Daignières  
101 et al. 1994). This area is also characterized by a major positive gravity anomaly regionally known as the  
102 Labourd anomaly (Casas et al. 1997; Chevrot et al. 2014) (Figs. 2A and 2C), which has been recently  
103 related to the presence of a mantle body in the basement of the northern part of the Mauléon basin  
104 (e.g. Jammes et al. 2009; Masini et al. 2014; Wang et al. 2016; Saspiturry et al. 2019b; Lescoutre &  
105 Manatschal 2020)(Fig. 2D). In spite of its importance to understand the rifting and orogenic evolutions,

106 the 3-D morphology of the continental Moho beneath the study area remains disputed (Daignières et al.  
107 1994; Chevrot et al. 2015; Wang et al. 2016; Teixell et al. 2018).

108 In this work, we exploit phase velocity maps of fundamental mode Rayleigh waves at periods  
109 between 2 and 9 s in order to invert a 3-D shear wave velocity ( $V_S$ ) model of the area. These phase  
110 velocity maps were obtained by extracting coherent surface wave fronts from seismic noise originat-  
111 ing from the Atlantic and Mediterranean sea using the Maupasacq array, as described in Lehujeur  
112 & Chevrot (2020). The method used an innovative matched-filtering technique to exploit the large  
113 number of seismological stations deployed simultaneously on the field and the strong directivity of  
114 ambient seismic noise. The present contribution can be seen as a continuation of that work as we in-  
115 vert the previously obtained phase velocity maps to image the 3-D variations of shear velocity beneath  
116 the Mauléon and Arzacq basins. The inversion procedure involves a first point-wise Markov Chain  
117 Monte-Carlo inversion (MCMC) to determine a 1-D shear velocity model at each surface node of the  
118 3-D tomographic grid. Then, these 1-D models are aggregated to get a preliminary 3-D model. This  
119 model is finally used to initiate a new 3-D iterative inversion, using a 3-D Gaussian model covariance  
120 matrix. This allows us to obtain a smooth 3-D model that fits the dispersion data.

121 The paper is organized as follows. In section 2, we provide an overview of the geological con-  
122 text of the study area highlighting the main questions that remain concerning the architecture of the  
123 Mauléon basin and his underlying basement. In section 3, we describe the details of the two-step  
124 surface-wave inversion method. In section 4, we confront and compare our  $V_S$  model derived from  
125 surface waves to other tomographic studies covering the area, and in particular to a recent local travel-  
126 time tomography that exploited the Maupasacq dataset. We also compare these models to constrained  
127 geological information from geological maps and well data. Finally, in section 5 after discussing the  
128 limits of passive imaging approaches, we propose a 3-D geological interpretation of the tomographic  
129 models.

## 130 2 GEOLOGICAL SETTING

### 131 2.1 Present-day Pyrenean structure

132 The Pyrenean mountain belt results from the north-south convergence between the Iberian and Eurasian  
133 plates from the Late Santonian to the Early Miocene (Puigdefàbregas & Souquet 1986; Olivet 1996;  
134 Rosenbaum et al. 2002; Macchiavelli et al. 2017; Van Hinsbergen et al. 2020). In its western part,  
135 the focus of this study, the belt is made of different structural units characterized by orogenic and  
136 pre-orogenic rift-related geological records (see Fig. 2B). The southern limit of the Aquitaine foreland  
137 basin is the North Pyrenean Frontal Thrust (NPFT), which corresponds to the Sainte-Suzanne thrust

138 in its westernmost part. Southward, the North Pyrenean Zone (NPZ) is separated from the Axial zone  
139 (AZ) by the south-verging Lakhoura thrust system. The AZ represents a large outcrop of exhumed  
140 Pre-Mesozoic rocks that hold some of the highest altitudes of the Pyrenees. It is connected to the  
141 South Pyrenean foreland basin (SPFB) by a set of south-verging thrusts. While the AZ and the SPFB  
142 mainly result from the Eocene-Miocene antiformal nappe-stacking of pre-orogenic Iberian thick con-  
143 tinental crust (proximal margin domains of Masini et al. (2014), Tugend et al. (2014) and Tugend et al.  
144 (2015)), the NPZ primarily results from the shortening of Cretaceous hyper-extended rift basins, with  
145 a basement-cover decoupling in the Upper Triassic evaporite layers. In the Western Pyrenees, the NPZ  
146 results from the inversion of the Mauléon Basin that has been thrust on top of the Aquitaine foreland  
147 basin. At the front of the NPFT, and buried underneath syn-orogenic sediments, the Arzacq rift basin  
148 corresponds to the northern extension of the Cretaceous Pyrenean rift system that escaped from most  
149 of the orogenic overprint (Masini et al. 2014; Tugend et al. 2015; Angrand et al. 2018; Issautier et al.  
150 2020; Ducoux et al. 2021).

## 151 **2.2 Tectono-stratigraphic evolution of the Western Pyrenees**

152 In the Western Pyrenees, the crustal basement is made of a complex lithological assemblage of pre-  
153 Mesozoic rocks. It includes metamorphic and sedimentary rocks that were variably affected by Variscan  
154 orogenic to post-orogenic deformations and intrusions (e.g. Saspiturry et al. 2019a). This complex in-  
155 herited crust was eroded and peneplained before being unconformably covered by continental clastics  
156 (Permian and Lower Triassic). An ill-defined early phase of rifting (see Leleu et al. 2016, for a review)  
157 was recorded through the Triassic marine transgression that eventually led to the deposition of the  
158 Upper Triassic evaporites (Curnelle 1983), which will represent the main *décollement* level during the  
159 subsequent rifting and orogenic deformations.

160 During the Jurassic, the Pyrenean domain recorded a quiet tectonic period through the devel-  
161 opment of a shallow marine carbonate platform (Canérot 2017). Another ill-defined pulse of rifting  
162 responsible for local emersion and erosion of the sedimentary cover is regionally recorded during the  
163 late Jurassic and early Cretaceous in the area (e.g. Canérot et al. 1999). The last and most intense  
164 rifting phase, the so-called hyper-extension phase, then occurred between the Aptian and the Ceno-  
165 manian. As the pre-orogenic crustal and basin architectures are mainly shaped by this hyper-extension  
166 phase of rifting, we will consistently refer to this latter phase by using a pre-, syn- and post-HE termi-  
167 nology ("HE" standing for "hyper-extension") to avoid any confusion with preceding rifting phases.  
168 While the precise kinematics of hyper-extension is still debated, it corresponds to the main phase of  
169 crustal thinning and accelerated subsidence within the Mauléon and Arzacq basins. Within the Maulón  
170 basin, this hyper-extension phase eventually led to the exhumation of the subcontinental mantle at the

171 seafloor during the early Cenomanian (Fig. 2D, Jammes et al. 2009; Masini et al. 2014; Saspiturry  
 172 et al. 2019b) and to the rework of mantle clasts within the syn-HE sediments (Fortané et al. 1986;  
 173 Jammes et al. 2009; Lagabrielle et al. 2010; Debrosas et al. 2010; Lagabrielle et al. 2019; Corre et al.  
 174 2016; Asti et al. 2019; Lagabrielle et al. 2019). Crustal thinning and tectonic exhumation of mantle  
 175 rocks were proposed to be accommodated by a set of long-offset detachment faults dipping either to  
 176 the north, to the south, or both, depending on the authors (Jammes et al. 2009; Masini et al. 2014;  
 177 Gómez-Romeu et al. 2019; Saspiturry et al. 2019b; Lescoutre et al. 2019).

178 After a short post-rift relaxation until the late Santonian, early orogenesis initiated with the inver-  
 179 sion of the Mauléon basin forming the early orogenic fold-and-thrust belt of the western Pyrenees.  
 180 During this stage, deformation was accommodated by the underthrusting of the former hyper-thinned  
 181 continental and exhumed mantle basement of the Mauléon basin underneath the European continen-  
 182 tal crust (Tugend et al. 2014; Mouthereau et al. 2014; Gómez-Romeu et al. 2019). At the surface,  
 183 part of the pre-HE sedimentary cover together with the syn- and post-HE cover were detached from  
 184 the hyper-extended basement (including Permian and Lower-Middle Triassic rocks) using the Keuper  
 185 evaporites as a basal *décollement* level. The Lakhora and NPFT fault systems thrust the deformed  
 186 sedimentary cover on top of both the Iberian and European continents (Jammes et al. 2009; Teixell  
 187 et al. 2016; Labaume & Teixell 2020). Following a Paleocene transitional phase of more diffuse defor-  
 188 mations (the "Pyrenean tectonic quiescence") and a Lower Eocene proto-collision stage (for details,  
 189 see Waldner et al. 2021; Teixell et al. 2016), shortening propagated further south from the Eocene to  
 190 the Miocene and formed the Pyrenean Axial Zone and the Iberian foreland fold and thrust belt (the  
 191 South Pyrenean Zone) up to the pro-foreland basin (the Ebro basin). While the collisional flexure was  
 192 also recorded on the European retro-foreland basin, shortening rates were more limited there in com-  
 193 parison to the southern side of the belt (e.g. Waldner et al. 2021; Teixell et al. 2016; Angrand et al.  
 194 2018). In the study area, syn-collisional deposits are lying underneath and northwards of the NPFT  
 195 (i.e. in the Aquitaine/Arzacq basins) as turbiditic deposits grading upsection to syn- and post-orogenic  
 196 marine and continental clastics. At depth, shortening was accommodated by the north-directed un-  
 197 derthrusting of the Iberian crust beneath Europe leading to the present-day imaged geometry of the  
 198 crustal root (Wang et al. 2016; Chevrot et al. 2018)(Fig. 2D).

### 199 **2.3 The non-cylindrical structure of the Western Pyrenees**

200 As introduced above, the structure of the NPZ and southern Aquitaine basin is mostly related to the  
 201 inversion of the Mauléon hyper-extended rift system. 2-D geological models generally state that the  
 202 thin-skinned shortening style recorded within the NPZ results from the decoupling created by the  
 203 evaporitic *décollement*, above which the cover got passively squeezed in a pop-up structure while



204 the basement was thickened by thrusts (Tugend et al. 2014; Mouthereau et al. 2014; Dumont et al.  
205 2015; Teixell et al. 2016; Labaume & Teixell 2020). If this evolution fits with first order observations  
206 in the eastern part of the Mauléon basin, sections and models proposed for the western side of the  
207 study area rather advocate a thick-skin crustal pop-up that sampled the autochthonous basement of the  
208 Mauléon basin within the orogenic wedge (e.g., Jammes et al. 2009; Masini et al. 2014; Lescoutre &  
209 Manatschal 2020; Saspiturry et al. 2020a). This pop-up structure is edged by the lateral continuations  
210 of the Lakhoura and NPFT systems in the south and north, respectively (Teixell et al. 2016; Lescoutre  
211 et al. 2021; Lescoutre & Manatschal 2020; Saspiturry et al. 2020a, Fig. 2D). It should be noticed that  
212 the sampled basement is outcropping within the Basque massifs forming the south-western margin of  
213 the Mauléon basin (Fig. 2B). There, it is made of Paleozoic rocks (with its pre-Keuper cover) to the  
214 south and of the Ursuya granulites to the north, the latter bearing a small body of serpentinized mantle  
215 (Boissonnas et al. 1974; Vielzeuf & Kornprobst 1984; Masini et al. 2014; Lescoutre 2019; Saspiturry  
216 2019; Saspiturry et al. 2019a). The pre-orogenic sediment draping of these basement rocks suggests  
217 that it corresponds to the autochthonous basement of the Mauléon basin, made of thinned continental  
218 crust and mantle rocks (Jammes et al. 2009; Masini et al. 2014; Wang et al. 2016; Chevrot et al. 2018;  
219 Lescoutre et al. 2021; Saspiturry et al. 2020a). The Labourd positive gravity anomaly in the western  
220 part of the Mauléon basin gives further support to this hypothesis (Figs. 2A and 2C). Although this  
221 anomaly was initially attributed to the presence of lower crustal rocks at shallow depth (Grandjean  
222 1994; Vacher & Souriau 2001; Pedreira et al. 2007), it has also been interpreted as a shallow piece  
223 of dense lithospheric mantle (Casas et al. 1997; Jammes et al. 2010). This interpretation has gained  
224 support from recent works documenting P-wave velocities of 7.3 km/s below 10 km depth (Fig. 2D,  
225 Wang et al. 2016; Chevrot et al. 2018). It was also observed that this gravity anomaly is progressively  
226 attenuating from west to east (Gottis 1972; Boillot et al. 1973, Fig. 2A), suggesting a structural and/or a  
227 lithological change across the basin (e.g. Masini et al. 2014, Fig. 2A). Lescoutre & Manatschal (2020)  
228 recently explained this structural change as reflecting the transition between shifted Mauléon-Arzacq  
229 and Basque-Cantabrian rift axes located north-east and south-west, respectively, of the Basque massifs  
230 (Fig. 2B). In this model the N20° orogen-perpendicular Saison and Barlanès transverse structures (TS;  
231 Rat 1988; Razin 1989; Masini et al. 2014; Saspiturry 2019; Lescoutre et al. 2021, Fig. 2B) played a  
232 significant role on the non-cylindrical structure of the Mauléon Basin. These structures divide the study  
233 area in 3 segments from west to east: the western and eastern Mauléon segments, and the Chainons  
234 Béarnais segment (Fig. 2B). The Saison structure is characterized by a steep dipping dextral shear  
235 zone (Zolnai 1975; Schoeffler 1982; Richard 1986; Saspiturry 2019), whereas the Barlanès structure  
236 corresponds to the lateral termination of the Chainons Béarnais folds. Even though they are assumed  
237 to be of fundamental importance for the closure of rifted domains during orogenesis (e.g. Lescoutre

238 & Manatschal 2020; Saspiturry 2019) their precise geometry and role at depth remain to be precised,  
239 which was one of the main motivations in the choice of the emplacement of the Maupasacq seismic  
240 acquisition used in this study.

## 241 3 METHODS

### 242 3.1 Surface wave tomography

243 The inversion of surface wave dispersion curves to determine the vertical variations of elastic pa-  
244 rameters (density, shear and compressional wave velocities) is a classical non-linear inverse problem  
245 commonly encountered in earthquake or ambient noise tomography. The forward problem can be  
246 efficiently computed using the propagator matrix method, which considers a superposition of homo-  
247 geneous layers over a half-space (e.g., Thomson 1950; Haskell 1953; Knopoff 1964; Gilbert & Backus  
248 1966; Aki & Richards 2002). The linearization of the problem has been extensively used to invert sur-  
249 face wave dispersion measurements because it is computationally efficient and can rapidly converge to  
250 a solution (e.g., Dorman & Ewing 1962; Xia et al. 1999). However, the inversion results may depend  
251 on the initial model. Due to the non-uniqueness of the solution, the lack of prior knowledge about the  
252 structures can therefore lead to very different models that fit the observations equally well (e.g., Bodet  
253 et al. 2005). Global search approaches such as grid search (e.g., Macquet et al. 2014), Monte-Carlo  
254 methods (e.g. Shapiro & Ritzwoller 2002; Socco & Boiero 2008; Maraschini & Foti 2010), genetic al-  
255 gorithms (e.g., Lomax & Snieder 1994), or neighborhood algorithms (Sambridge 1999; Mordret et al.  
256 2014) are thus often preferred since they only require solving a forward problem. In addition, they can  
257 also provide the posterior covariance matrix of the model.

258 Building a 3-D S-wave velocity model based on the phase velocity of surface waves is classically  
259 done by first estimating the local dispersion curves at each geographical location and then solving  
260 many independent 1-D inverse problems (e.g., Shapiro & Ritzwoller 2002). Other studies have pro-  
261 posed to integrate these two inversion problems into one to determine directly the 3-D structure either  
262 by linearized or Monte-Carlo methods (Fang et al. 2015; Zhang et al. 2018). These techniques still rely  
263 on the 1-D approximation for the forward computation of dispersion curves, but they allow controlling  
264 the lateral coherence of the velocity parameters.

265 In this work, we employ another two-step inversion scheme to invert a set of surface wave disper-  
266 sion maps at several periods, and we apply it to the Rayleigh waves phase velocity dispersion maps  
267 from Lehujeur & Chevrot (2020). In the first step, we invert the surface wave dispersion curves at each  
268 geographical location independently using a 1-D Markov chain Monte-Carlo inversion. This step pro-  
269 vides us a probability density function of the S-wave velocity as a function of depth at each location.

270 The median profiles are combined to form a preliminary 3-D S-wave velocity model. In the second  
 271 step, we perform a 3-D linearized inversion starting from the result of the point-wise inversion, and  
 272 we regularize the problem using a non-diagonal covariance matrix over the model space to smooth the  
 273 model laterally and vertically, while preserving the fit to the dispersion data.

### 274 3.1.1 Preliminary point-wise depth inversion

275 We first determine a preliminary model following the inversion approach described in Lehuteur et al.  
 276 (2018) except for some aspects that are detailed below. We invert the phase velocity dispersion curves  
 277 of fundamental mode Rayleigh waves sampled logarithmically at 9 periods between 2 and 9 s on the  
 278 surface nodes of the 3-D tomographic grid (Lehuteur & Chevrot 2020). We assume that the phase  
 279 velocity measurements at the 9 periods are independent. The 1-D models are described by the shear  
 280 velocity ( $V_S$ ) and thickness of 8 homogeneous layers overlying a half-space. The  $V_P$  and density inside  
 281 each layer, needed for the resolution of the forward problem are derived from  $V_S$ , using the  $V_P$ -to- $V_S$   
 282 and  $V_P$ -to-density scaling relationships given by Brocher (2005):

$$V_P = 0.9409 + 2.0947 V_S - 0.8206 V_S^2 + 0.2683 V_S^3 - 0.0251 V_S^4, \quad (1)$$

$$\rho = 1.6612 V_P - 0.4721 V_P^2 + 0.0671 V_P^3 - 0.0043 V_P^4 + 0.000106 V_P^5. \quad (2)$$

283 These relations are valid for  $V_S \leq 4.5$  km/s (eq. 1), and for  $1.5 \leq V_P \leq 8.5$  km/s (eq. 2). Here we  
 284 used them mostly to reduce the size of the model space to be explored by the Markov chain Monte-  
 285 Carlo algorithm, which reduces significantly the computational effort required by the first step of our  
 286 inversion procedure and does not impact the solution in a significant way as the Rayleigh waves are  
 287 mostly sensitive to  $V_S$  (e.g., Xia et al. 1999). The dispersion curves are computed with the codes from  
 288 Herrmann (2013). All the inverted parameters are restricted to a prescribed range using a uniform  
 289 probability density law, which reduces even more the size of the model space to explore and avoids  
 290 testing unrealistic models (see the area delimited with black dotted lines in Fig. 3). In addition, we  
 291 impose that the  $V_S$  variation between two consecutive layers are between -0.5 and +1.0 km/s. This  
 292 additional constraint forces the tested models to remain relatively smooth, while still allowing the  
 293 velocity to decrease with depth.

294 The inversions are run using 10 independent Markov chains launched in parallel. The proposal  
 295 distribution is adjusted during the inversion to maintain an acceptance rate of the Metropolis algo-  
 296 rithm around 25 %, and the Markov chains run until 2,500 models are kept, so that approximately  
 297 10,000 models are tested. We retain the median of the 1,000 best models found as the solution of the  
 298 inversion (Fig. 3). After combining all the median 1-D models, we obtained the 3-D S-wave velocity

299 model shown in Figs 4 and 5. The solutions at nearby locations are very consistent although the in-  
 300 verse problems are solved independently, which emphasizes the stability of the point-wise approach.  
 301 However, the small-scale irregularities suggest that the model is noisy. A simple cure would be to  
 302 smooth the model, but this would degrade the fit of observed data, as discussed later.

### 303 3.1.2 3-D inversion

304 To obtain the final 3-D  $V_S$  model, we perform a new linearized 3-D inversion, starting from the so-  
 305 lution obtained with the point-wise inversion described in the previous section, following the method  
 306 described in Montagner & Tanimoto (1990) for global surface-wave tomography. We regularize the  
 307 problem using a non-diagonal Gaussian 3-D covariance matrix to smooth the model, while preserving  
 308 the fit to the observations. The model is parameterized into a regular  $34 \times 23 \times 30$  Cartesian grid of  
 309  $1.612 \times 1.636 \times 0.345$  km size cells. As in the preliminary inversion,  $V_P$  and density are scaled to  
 310  $V_S$  using the relations from Brocher (2005) (Equations 1 and 2). The least squares cost function to  
 311 minimize is defined by (Tarantola & Valette 1982)

$$\chi^2(\mathbf{m}_n) = \chi_d^2(\mathbf{m}_n) + \chi_m^2(\mathbf{m}_n), \quad (3)$$

312 where

$$\chi_d^2(\mathbf{m}_n) = \frac{1}{2}[\mathbf{d}^{obs} - \mathbf{g}(\mathbf{m}_n)]^T \cdot \mathbf{C}_d^{-1} \cdot [\mathbf{d}^{obs} - \mathbf{g}(\mathbf{m}_n)], \quad (4)$$

$$\chi_m^2(\mathbf{m}_n) = \frac{1}{2}[\mathbf{m}_n - \mathbf{m}_0]^T \cdot \mathbf{C}_m^{-1} \cdot [\mathbf{m}_n - \mathbf{m}_0], \quad (5)$$

313  $\mathbf{d}^{obs}$  the data vector that contains the dispersion measurements,  $\mathbf{g}$  the operator that predicts the Rayleigh  
 314 wave dispersion curves,  $\mathbf{m}_n$  the model vector that contains the values of  $V_S$  inside each tomographic  
 315 grid cell,  $n$  the iteration number of the linearized inversion, and  $\mathbf{m}_0$  the starting  $V_S$  model. We assume  
 316 that all the measurements are independent and thus use a diagonal data covariance matrix  $\mathbf{C}_d$ . We also  
 317 assume that the spatial variations of  $V_S$  can be described by a Gaussian covariance matrix

$$\mathbf{C}_m = \sigma_m^2 \mathbf{S}, \quad (6)$$

318 where  $\sigma_m$  is the prior uncertainty on the  $V_S$  model assumed homogeneous and tuned to regularize the  
 319 inverse problem, and  $\mathbf{S}$  the Gaussian smoothing kernel

$$\mathbf{S}_{ij} = \exp \left\{ -\frac{1}{2} [(\mathbf{r}_i - \mathbf{r}_j)^T \cdot \mathbf{L}^{-1} \cdot (\mathbf{r}_i - \mathbf{r}_j)] \right\}. \quad (7)$$

where  $\mathbf{r}_i$  is the location of cell  $i$ . Because we expect a finer vertical resolution, we impose two distinct correlation lengths along the horizontal and vertical dimensions

$$\mathbf{L} = \begin{bmatrix} L_h^2 & & \\ & L_h^2 & \\ & & L_v^2 \end{bmatrix}, \quad (8)$$

where the horizontal ( $L_h$ ) and vertical ( $L_v$ ) correlation lengths are set to 2.5 km and 1 km, respectively.

This non-linear inverse problem is solved iteratively following Tarantola & Valette (1982), where the model is updated at each iteration according to

$$\mathbf{m}_{n+1} = \mathbf{m}_0 + \mathbf{C}_m \cdot \mathbf{G}_n^T (\mathbf{C}_d + \mathbf{G}_n \cdot \mathbf{C}_m \cdot \mathbf{G}_n^T)^{-1} \cdot [\mathbf{d}^{obs} - \mathbf{g}(\mathbf{m}_n) + \mathbf{G}_n \cdot (\mathbf{m}_n - \mathbf{m}_0)], \quad (9)$$

with  $\mathbf{G}_n$  the matrix containing the Fréchet derivatives computed in the current model  $\mathbf{m}_n$

$$\mathbf{G}_n(T, z) = \frac{\partial c(T)}{\partial V_s(z)} \Big|_{\mathbf{m}_n}. \quad (10)$$

where  $c$  denotes the phase velocity,  $V_s$  the S-wave velocity and  $T$  and  $z$  the period and depth respectively.

The inversion is initiated with  $\mathbf{m}_0$ , a smoothed version of the model  $\mathbf{m}^{prior}$  obtained in the preliminary inversion

$$\mathbf{m}_0 = \bar{\mathbf{S}} \cdot \mathbf{m}^{prior}, \quad (11)$$

where  $\bar{\mathbf{S}}_{ij} = \mathbf{S}_{ij} / \sum_k \mathbf{S}_{ik}$  is the normalized smoothing kernel. We run the second inversion step for several values of the prior uncertainty  $\sigma_m$ , used as a damping parameter. The inversion usually converges after 3 to 10 iterations depending on the damping coefficient used. The retained prior uncertainty is  $\sigma_m = 0.4$  km/s, slightly below the maximum curvature of the L-curve computed following Hansen & O’Leary (1993) (see the red dashed curve in Fig. 6).

The data misfit (first term of eq. (3)) obtained with the prior model resulting from point-wise inversion (step 1) is  $\chi_d^2(m^{prior}) = 169$  in arbitrary units (Fig. 6, blue dashed line). The starting model from eq. (11) has a much larger data misfit  $\chi_d^2(m_0) = 465$ , which demonstrates that simply smoothing the output of a point-wise inversion deteriorates the fit to dispersion data. After convergence of the second inversion, the data misfit for  $\sigma_m = 0.4$  km/s is  $\chi_d^2(m^{sol}) = 124$  (Fig. 6), which is lower than the misfit obtained with the prior model. Examples of observed and modeled dispersion curves for the prior, starting, and optimized models are shown in Fig. 7.

### 3.2 Local Earthquake tomography

In order to provide independent constraints on the S-wave velocity structure we also show the results of a  $V_S$  model obtained from local earthquake tomography (Villaseñor et al. 2019) using arrival times picked on records from the stations of the Maupasacq experiment. During the 6 months of operation of this temporary network, a total of 1980 local earthquakes were detected and located (Polychronopoulou et al. 2018). From this catalog we selected for the tomography well recorded earthquakes with at least 8 P arrival times, 2 S arrival times and an azimuthal gap smaller than 200 degrees. This resulted in a dataset consisting of 996 earthquakes with a total of 87,122 P-wave and 72,445 S-wave arrival times.

The tomographic inversion method used is based on Benz et al. (1996) as modified by Tryggvason et al. (2002) in order to incorporate P- and S-wave arrival times. The travel times (forward problem) are calculated using the finite-difference code of Podvin & Lecomte (1991), which provides accurate results even for models with large lateral variations in velocity structure. The tomographic method inverts simultaneously for P- and S-wave velocity structure and earthquake relocation. This is a non-linear inverse problem so in order to find its solution it is first linearized and then solved iteratively. The model is parameterized in terms of constant velocity cells of 1.2 x 1.2 x 1.2 km in size, and the dimensions of the model region are 130 km and 115 km along the E-W and N-S directions respectively.

The starting model used in the inversion is the 1-D velocity model previously determined for earthquake location (Polychronopoulou et al. 2018). The final model shown here was obtained after 10 iterations. The initial root-mean square (RMS) error of the used arrival times was 0.107 s for P waves and 0.101 s for S waves, and the final RMS was 0.082 s for P waves and 0.081 s for S waves. This represents a variance reduction of 23% for P waves and 20% for S waves, which is typical for travel time tomography. We estimated the resolving power of the dataset performing reconstruction tests of synthetic checkerboard models (supplementary materials S3). Due to the high density of stations, we were able to resolve reliably anomalies of 5 km in size and larger in the center of the LET model (southern part of the Maupasacq deployment), where the high velocity anomalies of interest are located.

The S-wave velocity model obtained using local earthquake tomography shows finer details than the one obtained from SWT in the regions that are well sampled by crossing rays. However large regions of the model that are not illuminated by rays are unconstrained. This problem is less significant in surface wave tomography because of the characteristics of the sensitivity of surface waves. Similarly the actual value of the velocity anomalies obtained from local earthquake tomography is typically overestimated, while the values obtained from surface waves are more realistic. Therefore, combining

375 the complementary characteristics of both methods we can better describe the features of the seismic  
376 velocity structure.

#### 377 **4 THE TOMOGRAPHIC MODELS**

378 The final  $V_S$  model obtained after inversion of the surface wave dispersion curves is shown in Figs  
379 8 and 9. As expected, this model is smoother than the prior model shown in Figure 4 but the domi-  
380 nant structures are very similar. Figure 10 displays  $V_S$  at 1 km depth in our surface-wave tomography  
381 (SWT) model and in the local earthquake tomography (LET)  $V_S$  model described here and in Vil-  
382 laseñor et al. (2019). Whereas these two models were derived from completely independent datasets,  
383 they show very similar and coherent velocity structures. For example, both models image higher than  
384 average velocities in the Mauléon basin (SW part in the map shown in Fig. 10). However, the average  
385 velocity in the LET model is clearly on average faster than in the SWT model. Figures 11-13 show  
386 cross-sections in the SWT and LET models. These vertical cross-sections are also in good agreement,  
387 but the vertical resolution is finer in the SWT model than in the LET model, especially in the area of  
388 the Arzacq basin (Fig. 11). For example, the expected top of the basement of the Arzacq basin (ca. 3  
389 km in depth on the northern part of the Fig. 11) is more sharply defined in the SWT model whereas the  
390 LET model shows a more gradual transition. In contrast, the LET model has a finer lateral resolution  
391 compared to the SWT model, especially at depths larger than 6 km.

392 Both models show anomalies that are in good agreement with surface geology. For example, the  
393 elliptical low velocity anomaly observed in both models in the central part of the Mauléon basin and  
394 elongated along the WNW-ESE direction (y1 in Figs. 10, 12 and 13), i.e. parallel to the strike of the  
395 main orogenic structures, corresponds to the core of a mapped syncline. The core of this syncline is  
396 filled by Upper Cretaceous turbidites with Lower Cretaceous and Jurassic marls and limestones under-  
397 neath. Conversely, the Saint Palais anticline in the central part of the C1-C3 section is characterized  
398 by higher seismic velocities (y2 in Figs. 10 and 13). The low velocity anomaly y3 in Figs. 10 and  
399 11, seen in both models, is related to the Cenozoic sediments accumulated in the Aquitaine basin. On  
400 map view, the regional shape of the NPFT, which juxtaposes Mesozoic rocks onto younger sediments  
401 and makes a lateral ramp north of the Saison structure, has a clear signature at shallow depth in both  
402 models (y4 in Fig. 10). Finally, the higher velocities in the southern part of the models can be related  
403 to the metamorphic rocks of the Arbailles and Labourd Paleozoic massifs (Figs. 10).

404 In figures 14-16, we compare our tomographic models with seismic reflection profiles, surface  
405 geology and well data from some key boreholes of the Mauléon basin (details in supplementary ma-  
406 terials S1 and S2). In order to facilitate these comparisons, we converted our models from depth to  
407 two-way travel times using

$$\text{twt}(x, z) = 2 \left[ \int_{z_{\text{topo}}}^z \frac{dy}{V_P(x, y)} + \frac{z_{\text{topo}} - z_{\text{srd}}}{V_{\text{rep}}} \right]. \quad (12)$$

408 where  $\text{twt}(x, z)$  is the two-way travel time corresponding to depth  $z$  and position  $x$  along the profile,  
 409  $V_P$  the P-wave velocity estimated by multiplying the  $V_S$  by a  $V_P/V_S$  ratio of 1.73,  $z_{\text{srd}}$  the reference  
 410 level taken at 500 m above the sea level,  $z_{\text{topo}}$  the topography level, and  $V_{\text{rep}}$  the replacement velocity  
 411 chosen at 2.5 km/s. The time adjustment related to  $z_{\text{srd}}$  and  $V_{\text{rep}}$  is used to avoid propagating the  
 412 irregular surface topography in the twt profile. It consists in filling the volume between the topography  
 413 and the reference level by an imaginary layer of constant velocity. The values chosen for  $V_{\text{rep}}$  and  $z_{\text{srd}}$   
 414 have little impact on the resulting figures.

415 In the central part of the western section (Fig. 15), a velocity inversion is observed at  $\sim 2$  s TWT  
 416 in the SWT model (Fig. 15A). This inversion is in good agreement with the Bellevue well, which doc-  
 417 uments Jurassic marls and limestones over the imbricated Lower Cretaceous limestones and Upper  
 418 Triassic evaporites (Fig. S1). This tectonic contact probably corresponds to the Bellevue thrust that is  
 419 cropping out at the surface further north. A similar velocity inversion can be recognized in the northern  
 420 part of the SWT model on the western section at 2.5 s TWT. This depth corresponds to the occur-  
 421 rence of the Sainte-Suzanne thrust in the Orthez well that brings shallow high-velocity rocks (Lower  
 422 Cretaceous and Jurassic carbonates) on top of younger clastics sediments (Fig. S1). Further south, a  
 423 shallow and smooth vertical velocity inversion can also be observed north of the Arbailles massif,  
 424 where the nearby Ainhice well documented a duplication of the stratigraphy at depth (Lescoutre et al.  
 425 2019, 2021; Saspiturry et al. 2019b, Fig. S1). This structure could correspond to a thin-skin thrust at  
 426 the front of the Arbailles massif (Fig. 15).

## 427 5 DISCUSSION

### 428 5.1 Limits of passive imaging methods

429 Part of the resolution discrepancy observed between SWT and LET may be explained from the differ-  
 430 ent parameterization and regularization schemes used in the two types of inversions. However, because  
 431 velocity anomalies tend to be smeared along the propagation directions, surface waves better constrain  
 432 vertical structural variations compared to horizontal ones, whereas for body waves it is the opposite.  
 433 Vertical smearing is indeed strongly expressed in the LET model, particularly at shallow depth. This  
 434 may partly explain the smaller amplitudes of velocity anomalies in the upper crust in this model. The  
 435 comparison of LET and SWT also reveals that whereas the shallow velocity anomalies in the two mod-  
 436 els are rather well correlated, the LET model is on average faster than the SW model. This suggests  
 437 that the starting 1-D model used in the LET inversion is on average too fast, a bias that remains in the



438 final 3-D model. This can simply be understood by the trade-off between the average velocity model  
439 and the origin time of the earthquakes. Therefore, the initial model used in LET still has a strong  
440 imprint on the final 3-D model, and it is thus crucial to build this model very carefully, using all the a  
441 priori information that is available. SWT could provide such key constraints on absolute velocities, in  
442 particular at shallow levels.

443 Other important differences come from the intrinsic limitations of both approaches. In LET, the  
444 resolution is controlled by ray coverage, and thus by the distribution of earthquakes. In the western  
445 Pyrenees, the seismicity is concentrated inside a narrow band that approximately follows the limit  
446 between the Axial Zone and the North Pyrenean Zone, with hypocentral depths rarely exceeding  
447 20 km (Souriau & Pauchet 1998; Chevrot et al. 2011). Owing to the distribution of earthquakes, the  
448 resolution is thus limited to the top 15 km, but it degrades notably beneath the Arzacq basin at depths  
449 below 10 km. In contrast, the main limitation of SWT comes from the amplitude and distribution  
450 of noise sources, the geometry of the array, and the sensor types. In this study, we exploited surface  
451 waves excited by energetic oceanic sources at periods from 2 to 9 s (microseismic band). At longer  
452 period, the sensitivities of geophones and short period sensors become very low, and the records are  
453 dominated by instrumental noise. Therefore, at periods longer than  $\sim 6$  s only the broadband sensors  
454 can be exploited. In addition, the wavelengths of Rayleigh waves at these periods are larger than 20 km,  
455 i.e. of the order of the size of the region that we want to image. This may explain the degradation of  
456 the lateral resolution in the deeper part of the model, especially beneath the NW-SE Mauléon transect  
457 shown in Figure 12. On the other hand, at shorter period the station spacing ( $\geq 1$  km) becomes too  
458 coarse to sample the wavefield with at least 2 samples per wavelength, and cycle skipping issues  
459 appear. For these reasons, the resolution is more uniform in the SWT model but limited to the top  
460 10 km of the crust.

461 In any case, the similarity of LET and SWT models, in addition to the different but complemen-  
462 tary sensitivity of body and surface waves to shallow structures, suggest that joint inversions would  
463 be a natural way to further improve the resolution and robustness of crustal tomographic models.  
464 Because these inverse problems are still solved separately with different model parameterization and  
465 regularization schemes, this will require developing a new generation of inversion codes.

## 466 **5.2 Geological interpretations and integration into a 3-D structural model**

467 We now attempt to build a coherent 3-D model of the Mauléon basin. We base our interpretation  
468 mostly on the shape of the velocity anomalies observed in the new tomographic models and how these  
469 anomalies agree or not with the available geological information, gravity data and seismic profiles,  
470 keeping in mind the strengths and weaknesses of each approach discussed above. As already pointed

471 out in the previous section, the velocity inversions can be associated with major thrusts (see section 4;  
472 Fig. 15). The inversion seen on the eastern section (Fig. 14) can thus be interpreted as the southward  
473 continuation of the south-dipping NPFT beneath the bottom of the Les-Cassières-2 borehole (Fig. S2).

474 The western profile is located to the west of the Saison structure (Fig. 2A), where the positive  
475 Bouguer gravity anomaly interpreted as related to a shallow body of subcontinental mantle has been  
476 imaged by Wang et al. (2016). This piece of mantle is located in the hanging-wall of the Sainte Suzanne  
477 thrust (Fig. 15). East of the Saison structure, the high velocity mantle body is laterally shifted to the  
478 south and replaced by lower velocity rocks in the hanging wall of the steeper NPFT. These rocks might  
479 correspond to middle/lower crustal (metamorphic) rocks, serpentinized mantle or sedimentary rocks.  
480 The geometry of the iso-velocity lines at depth, in both the eastern and western NS sections, suggests  
481 that the high-velocity rocks ( $V_S > 3.8$  km/s) get shallower towards the north underneath the Mauléon  
482 basin, and thus that upper crustal rocks thin at the expense of deeper lithospheric rocks. Note that  
483 similar relationships between basement velocities and crustal tapering were reported from offshore  
484 Ocean-Continent transitions such as the Iberian (Dean et al. 2000) or the Newfoundland (Lau et al.  
485 2006) margins. This interpretation is in line with previous models from the Mauléon basin involving  
486 north-dipping detachment faults exhuming granulite and subcontinental mantle rocks (Jammes et al.  
487 2009; Masini et al. 2014; Gómez-Romeu et al. 2019; Saspiturry et al. 2019b; Lescoutre et al. 2019).

488 In the along-strike section (Fig. 16), the 3.2-3.6 km/s iso-velocity lines become shallower at the  
489 western edge of the LET profile where the basement rocks of the Labourd massif are cropping out  
490 (Fig. 2B). The trend of these iso-velocity lines indicate the geometry of the top basement at depth.  
491 At the eastern edge of the E-W section, the high velocities at shallow depth are in good agreement  
492 with the nappe-stack of the Chaînons Béarnais that consists of mixed sedimentary cover (including  
493 metamorphosed carbonates) and basement rocks (including serpentinized mantle bodies) (Labaume &  
494 Teixell 2020). At depth, in the central part of the model, a steep velocity contrast between high veloc-  
495 ities to the west and lower velocities to the east can be observed on the LET model (Fig. 16). In the  
496 easternmost part of the E-W profile, a similar observation can be made with an abrupt change towards  
497 lower velocities to the east. These steep velocity gradients correspond to the location at depth of the  
498 Saison and Barlanès transverse structures mapped at the surface (Fig. 2B). Therefore, these structures  
499 are segmenting the Mauléon basin and the Chainons Béarnais in a roughly orogen-perpendicular di-  
500 rection. As seismic velocities are to first-order positively correlated to densities, this observation is  
501 consistent with the eastward attenuation of the positive gravity anomaly attributed to shallow mantle  
502 rocks across the Saison and Barlanès structures (Figs. 2A and 12). The exact nature of the basement  
503 rocks and the depth of the Moho on both sides of the Saison structure remain poorly constrained.  
504 However, as stated above, the tomographic model of Wang et al. (2016) suggests the presence of sub-

505 continental mantle at shallow depth ( $\sim 10$  km) below the western Mauléon segment. Because the LET  
506 model shows relatively lower velocities from the west to the east of the Saison structure, and the grav-  
507 ity anomaly shows a similar transition (Fig. 12), the basement of the eastern Mauléon segment is most  
508 likely made of less dense material more altered/serpentinized (e.g. mantle rocks or mafic/metamorphic  
509 lower crust). This interpretation is in good agreement with previous structural models that interpreted  
510 the Saison structure as a crustal transfer zone active during the Pyrenean orogeny (Masini et al. 2014;  
511 Lescoutre & Manatschal 2020; Saspiturry 2019). The Saison and Barlanès structures accommodated  
512 deformation between the western Mauléon segment, where the hyperextended rift domain together  
513 with the subcontinental mantle rocks have been transported in the hanging wall of a north-vergent  
514 thrust, and the Chainons Béarnais segment, where most of this hyperextended domain has been under-  
515 thrusted beneath the European crust (Fig. 17). This distributed deformation also suggests a change in  
516 the structural level of indentation during the orogeny. While the European crust anomalously indented  
517 the Iberian mantle at an early stage of convergence in the west leading to its shallow sampling (i.e.  
518 thick-skinned style, see Lescoutre & Manatschal 2020), it is likely that the indentation rather used  
519 the basement-sediment interface in the east (Fig. 17). This scenario explains the apparent increase of  
520 thin-skinned shortening eastward, because of a significant accommodation of shortening within the  
521 basement in the west. Note that these complex 3-D structures are restricted to the hanging-wall of the  
522 north-dipping “slab” previously imaged by Wang et al. (2016) that should be consistently made of the  
523 Iberian basement formerly located in the southern border of the basin.

## 524 **6 CONCLUSION**

525 Our study demonstrates that, using dense large-N deployments, it is possible to obtain finely resolved  
526 images of fold and thrust belts from the exploitation of surface and body waves with passive imag-  
527 ing approaches. Obviously, the level of details in our tomographic images is not on par with a typ-  
528 ical seismic reflection survey and resolving the different sedimentary horizons inside a sedimentary  
529 basin is clearly beyond the reach of surface wave tomography. Nevertheless, our study provides ro-  
530 bust first-order constraints on the deep architecture of the Mauléon and Arzacq basins, where previous  
531 controlled source seismic reflection studies actually gave rather poor results, and for a fraction of  
532 the cost of such acquisitions. In particular, our tomographic models confirm the presence of orogen-  
533 perpendicular structures in the study area that controlled the along-strike change in the orogenic base-  
534 ment structure and composition. They also control the local preservation of hyper-extended rifted crust  
535 and mantle at shallow depth going along the gravimetric anomaly. We are thus convinced that passive  
536 imaging represents a valuable source of information that should be considered in the future, especially  
537 in environments where controlled source acquisitions are challenging or are impeded by legislation.

538 **ACKNOWLEDGMENTS**

539 This work was supported by OROGEN, a tripartite research project between the CNRS, TOTAL and  
540 BRGM, and by the ANR AAPG program (project CLEARVIEW, ANR-17-CE23-0022). AV received  
541 funding from the Spanish government through the ‘Severo Ochoa Centre of Excellence’ accreditation  
542 (CEX2019-000928-S). We thank associate editor David Pedreira, as well as Josep Antón Muñoz and  
543 an anonymous reviewer for their constructive comments.

544 **REFERENCES**

- 545 Aki, K. & Richards, P. G., 2002. *Quantitative Seismology*, University Science Books.
- 546 Angrand, P., Ford, M., & Watts, A. B., 2018. Lateral variations in foreland flexure of a rifted continental  
547 margin: The aquitaine basin (sw france), *Tectonics*, **37**(2), 430–449.
- 548 Asti, R., Lagabrielle, Y., Fourcade, S., Corre, B., & Monié, P., 2019. How do continents deform during man-  
549 tle exhumation? insights from the northern iberia inverted paleopassive margin, western pyrenees (france),  
550 *Tectonics*, **38**(5), 1666–1693.
- 551 Benz, H. M., Chouet, B. A., Dawson, P. B., Lahr, J. C., Page, R. A., & Hole, J. A., 1996. Three dimensional  
552 P and S wave velocity structure of Redoubt volcano, Alaska, *Journal of Geophysical Research*, **101**(B4),  
553 8111–8128.
- 554 Bodet, L., van Wijk, K., Bitri, A., Abraham, O., Côte, P., Grandjean, G., & Leparoux, D., 2005. Surface-  
555 wave inversion limitations from laser-doppler physical modeling, *Journal of Environmental & Engineering*  
556 *Geophysics*, **10**(2), 151–162.
- 557 Boillot, G., Capdevilla, R., Hennequin-Marchand, I., Lamboy, M., & Lepretre, J. P., 1973. La zone nord-  
558 pyrénéenne, ses prolongements sur la marge continentale nord-espagnole et sa signification structurale,  
559 *Comptes rendus de l'Academie des sciences (Paris)*, **227**, 2629–2632.
- 560 Boissonnas, J., Destombes, J., Heddebaut, C., Le Pochat, G., Lorsignol, S., Roger, P., & Ternet, Y., 1974.  
561 Feuille de iholdy (1027), carte géologique de la france, scale 1/50,000, *Bureau de Recherche Géologique et*  
562 *Minières*.
- 563 Brocher, T. M., 2005. Empirical relations between elastic wavespeeds and density in the earth's crust, *Bulletin*  
564 *of the seismological Society of America*, **95**(6), 2081–2092.
- 565 Canérot, 2017. The pull apart-type tardets-mauléon basin, a key to understand the formation of the pyrenees,  
566 *Bull. Soc. géol. Fr.*, **188**(6), 35.
- 567 Canérot, J., Majesté-Menjoulas, C., & Ternet, Y., 1999. Le cadre stratigraphique et géodynamique des altérites  
568 et des bauxites sur la marge ibérique des pyrénées occidentales (france), *Comptes Rendus de l'Académie des*  
569 *Sciences - Series IIA - Earth and Planetary Science*, **328**(7), 451–456.
- 570 Casas, A., Kearey, P., Rivero, L., & Adam, C. R., 1997. Gravity anomaly map of the Pyrenean region and  
571 a comparison of the deep geological structure of the western and eastern Pyrenees, *Earth and Planetary*  
572 *Science Letters*, **150**(1-2), 65–78.
- 573 Chevrot, S., Sylvander, M., & Delouis, B., 2011. A preliminary catalogue of moment tensors for the Pyrenees,  
574 *Tectonophysics*, **510**, 239–251.
- 575 Chevrot, S., Villaseñor, A., Sylvander, M., & The Pyrope Team, 2014. High resolution imaging of the Pyrenees  
576 and Massif Central from the data of the PYROPE and IBERARRAY portable array deployments, *J. Geophys.*  
577 *Res.*, **119**(8), 6399–6420, doi: 10.1002/2014JB010953.
- 578 Chevrot, S., Sylvander, M., Diaz, J., Ruiz, M., Paul, A., & the PYROPE Working group, 2015. The Pyrenean  
579 architecture as revealed by teleseismic P-to-S converted waves recorded along two dense transects, *Geophys.*  
580 *J. Int.*, **200**, 1096–1107.

- 581 Chevrot, S., Sylvander, M., Diaz, J., Martin, R., Mouthereau, F., Manatschal, G., Masini, E., Calassou, S., Gri-  
 582 maud, F., Pauchet, H., & Ruiz, M., 2018. The non-cylindrical crustal architecture of the Pyrenees, *Scientific*  
 583 *Reports*, **8**(1), 9591.
- 584 Corre, B., Lagabrielle, Y., Labaume, P., Fourcade, S., Clerc, C., & Ballèvre, M., 2016. Deformation associated  
 585 with mantle exhumation in a distal, hot passive margin environment: New constraints from the Sarailié Massif  
 586 (Chaînons Béarnais, North-Pyrenean Zone), *Comptes Rendus Geoscience*, **348**(3-4), 279–289.
- 587 Curnelle, R., 1983. Evolution structuro-sédimentaire du trias et de l’infra-lias d’aquitaine, *Bulletin des Centres*  
 588 *de recherches exploration-production Elf-Aquitaine*, **7**(1), 69–99.
- 589 Daignières, M., Séguret, M., Specht, M., & ECORS Team, 1994. The Arzacq-Mauléon-Western Pyrenees  
 590 ECORS Deep Seismic Profile, in *Hydrocarbon and Petroleum Geology of France*, vol. 4 of **Eur. Assoc. Pet.**  
 591 **Geosci. Spec. Publ.**, pp. 199–208, ed. Mascle, A., Springer-Verlag, Academic, USA.
- 592 Dean, S., Minshull, T., Whitmarsh, R., & Louden, K., 2000. Deep structure of the ocean-continent transition  
 593 in the southern Iberia abyssal plain from seismic refraction profiles: The IAM-9 transect at 40° 20' N, *Journal*  
 594 *of Geophysical Research: Solid Earth*, **105**(B3), 5859–5885.
- 595 Debroas, E. J., Canérot, J., & Bilotte, M., 2010. Les brèches d’Urdach, témoins de l’exhumation du manteau  
 596 pyrénéen dans un escarpement de faille vraconnien-cénomaniens inférieur (Zone nord-pyrénéenne, Pyrénées-  
 597 Atlantiques, France), *Géologie de la France*, **2**, 53–63.
- 598 Dorman, J. & Ewing, M., 1962. Numerical inversion of seismic surface wave dispersion data and crust-mantle  
 599 structure in the New York-Pennsylvania area, *Journal of Geophysical Research*, **67**(13), 5227–5241.
- 600 Ducoux, M., Masini, E., Tugend, J., Gómez-Romeu, J., & Calassou, S., 2021. Basement-decoupled hyper-  
 601 extension rifting: The tectono-stratigraphic record of the salt-rich pyrenean necking zone (Arzacq basin, SW  
 602 France), *GSA Bulletin*.
- 603 Dumont, T., Replumaz, A., Rouméjon, S., Briais, A., Rigo, A., & Bouillin, J.-P., 2015. Microseismicity of  
 604 the Béarn range: reactivation of inversion and collision structures at the northern edge of the Iberian plate,  
 605 *Tectonics*, **34**(5), 934–950.
- 606 Fang, H., Yao, H., Zhang, H., Huang, Y.-C., & van der Hilst, R. D., 2015. Direct inversion of surface wave  
 607 dispersion for three-dimensional shallow crustal structure based on ray tracing: methodology and application,  
 608 *Geophysical Journal International*, **201**(3), 1251–1263.
- 609 Fortané, A., Duée, G., Lagabrielle, Y., & Coutelle, A., 1986. Lherzolites and the western “Chaînons Béarnais”  
 610 (French Pyrenees): Structural and paleogeographical pattern, *Tectonophysics*, **129**(1-4), 81–98.
- 611 Gassenmeier, M., Sens-Schönfelder, C., Delatre, M., & Korn, M., 2014. Monitoring of environmental influ-  
 612 ences on seismic velocity at the geological storage site for CO<sub>2</sub> in Ketzin (Germany) with ambient seismic  
 613 noise, *Geophysical Journal International*, **200**(1), 524–533.
- 614 Gilbert, F. & Backus, G. E., 1966. Propagation matrices in elastic wave and vibration problems, *Geophysics*,  
 615 **31**(2), 326–332, Publisher: GeoScienceWorld.
- 616 Gottis, M., 1972. Construction d’un modèle géodynamique pyrénéen, *Comptes Rendus Académie des Sciences*,  
 617 **275**.

- 618 Grandjean, G., 1994. Etude des structures crustales dans une portion de chaîne et de leur relation avec les  
619 bassins sédimentaires. Application aux Pyrénées occidentales, *Bull. Cent. Rech. Explor. Prod. Elf Aquitaine*,  
620 **18**(2), 391–420.
- 621 Gómez-Romeu, J., Masini, E., Tugend, J., Ducoux, M., & Kusznir, N., 2019. Role of rift structural inheritance  
622 in orogeny highlighted by the Western Pyrenees case-study, *Tectonophysics*, **766**, 131–150.
- 623 Hansen, P. C. & O’Leary, D. P., 1993. The use of the l-curve in the regularization of discrete ill-posed problems,  
624 *SIAM journal on scientific computing*, **14**(6), 1487–1503.
- 625 Haskell, N. A., 1953. The dispersion of surface waves on multilayered media, *Bulletin of the Seismological*  
626 *Society of America*, **43**(1), 17–34.
- 627 Herrmann, R. B., 2013. Computer programs in seismology: An evolving tool for instruction and research,  
628 *Seismological Research Letters*, **84**(6), 1081–1088.
- 629 Issautier, B., Saspiturry, N., & Serrano, O., 2020. Role of structural inheritance and salt tectonics in the  
630 formation of pseudosymmetric continental rifts on the european margin of the hyperextended Mauléon basin  
631 (Early Cretaceous Arzacq and Tartas Basins), *Marine and Petroleum Geology*, **118**, 104395.
- 632 Jammes, S., Manatschal, G., Lavier, L., & Masini, E., 2009. Tectonosedimentary evolution related to extreme  
633 crustal thinning ahead of a propagating ocean: Example of the western Pyrenees, *Tectonics*, **28**, TC4012,  
634 doi:10.1029/2008TC002406.
- 635 Jammes, S., Tiberi, C., & Manatschal, G., 2010. 3D architecture of a complex transcurrent rift system: The  
636 example of the Bay of Biscay–Western Pyrenees, *Tectonophysics*, **489**(1-4), 210–226.
- 637 Jia, Z. & Clayton, R. W., 2021. Determination of Near Surface Shear-Wave Velocities in the Central Los  
638 Angeles Basin With Dense Arrays.
- 639 Knopoff, L., 1964. A matrix method for elastic wave problems, *Bulletin of the Seismological Society of*  
640 *America*, **54**(1), 431–438.
- 641 Labaume, P. & Teixell, A., 2020. Evolution of salt structures of the Pyrenean rift (Chaînons Béarnais, France):  
642 From hyper-extension to tectonic inversion, *Tectonophysics*, **785**, 228451.
- 643 Lagabrielle, Y., Labaume, P., & de Saint Blanquat, M., 2010. Mantle exhumation, crustal denudation, and  
644 gravity tectonics during Cretaceous rifting in the Pyrenean realm (SW Europe): Insights from the geological  
645 setting of the lherzolite bodies, *Tectonics*, **29**(4).
- 646 Lagabrielle, Y., Asti, R., Fourcade, S., Corre, B., Poujol, M., Uzel, J., Labaume, P., Clerc, C., Lafay, R.,  
647 Picazo, S., & Maury, R., 2019. Mantle exhumation at magma-poor passive continental margins. Part I. 3D  
648 architecture and metasomatic evolution of a fossil exhumed mantle domain (Urdach lherzolite, north-western  
649 Pyrenees, France), *BSGF - Earth Sciences Bulletin*, **190**, 8.
- 650 Lau, K. H., Loudon, K. E., Funck, T., Tucholke, B. E., Holbrook, W. S., Hopper, J. R., & Christian Larsen, H.,  
651 2006. Crustal structure across the grand banks—newfoundland basin continental margin—i. results from a  
652 seismic refraction profile, *Geophysical Journal International*, **167**(1), 127–156.
- 653 Lehuteur, M. & Chevrot, S., 2020. Eikonal tomography using coherent surface waves extracted from ambient  
654 noise by iterative matched filtering—application to the large-n maupasacq array, *Journal of Geophysical*

- 655 *Research: Solid Earth*, **125**(6).
- 656 Lehujeur, M., Vergne, J., Schmittbuhl, J., Zigone, D., Le Chenadec, A., & Team, E., 2018. Reservoir imaging  
657 using ambient noise correlation from a dense seismic network, *Journal of Geophysical Research: Solid Earth*,  
658 **123**(8), 6671–6686.
- 659 Leleu, S., Hartley, A. J., van Oosterhout, C., Kennan, L., Ruckwied, K., & Gerdes, K., 2016. Structural,  
660 stratigraphic and sedimentological characterisation of a wide rift system: The triassic rift system of the central  
661 atlantic domain, *Earth-Science Reviews*, **158**, 89–124.
- 662 Lescoutre, R., 2019. *Formation et réactivation du système de rift pyrénéo-cantabrique: héritage, segmentation*  
663 *et évolution thermique*, Ph.D. thesis, Strasbourg.
- 664 Lescoutre, R. & Manatschal, G., 2020. Role of rift-inheritance and segmentation for orogenic evolution:  
665 example from the Pyrenean-Cantabrian system, *BSGF - Earth Sciences Bulletin*, **191**, 18.
- 666 Lescoutre, R., Tugend, J., Brune, S., Masini, E., & Manatschal, G., 2019. Thermal Evolution of Asymmetric  
667 Hyperextended Magma-Poor Rift Systems: Results From Numerical Modeling and Pyrenean Field Observa-  
668 tions, *Geochemistry, Geophysics, Geosystems*, **20**(10), 4567–4587.
- 669 Lescoutre, R., Manatschal, G., & Muñoz, J. A., 2021. Nature, origin and evolution of the pyrenean-cantabrian  
670 junction, *Tectonics*, **n/a**(n/a), e2020TC006134, e2020TC006134 2020TC006134.
- 671 Lin, F. C., Moschetti, M. P., & Ritzwoller, M. H., 2008. Surface wave tomography of the western United  
672 States from ambient seismic noise: Rayleigh and Love wave phase velocity maps, *Geophysical Journal In-*  
673 *ternational*, **173**(1), 281–298.
- 674 Lomax, A. & Snieder, R., 1994. Finding sets of acceptable solutions with a genetic algorithm with applica-  
675 tion to surface wave group dispersion in Europe, *Geophysical Research Letters*, **21**(24), 2617–2620, eprint:  
676 <https://agupubs.onlinelibrary.wiley.com/doi/pdf/10.1029/94GL02635>.
- 677 Lu, Y., Stehly, L., & Paul, A., 2018. High-resolution surface wave tomography of the European crust and  
678 uppermost mantle from ambient seismic noise, *Geophysical Journal International*, **214**(2), 1136–1150, Pub-  
679 lisher: Oxford Academic.
- 680 Macchiavelli, C., Vergés, J., Schettino, A., Fernández, M., Turco, E., Casciello, E., Torne, M., Pierantoni, P. P.,  
681 & Tunini, L., 2017. A new southern north atlantic isochron map: Insights into the drift of the iberian plate  
682 since the late cretaceous, *Journal of Geophysical Research: Solid Earth*, **122**(12), 9603–9626.
- 683 Macquet, M., Paul, A., Pedersen, H. A., Villaseñor, A., Chevrot, S., Sylvander, M., & Wolyniec, D., 2014.  
684 Ambient noise tomography of the Pyrenees and the surrounding regions: inversion for a 3-D Vs model in the  
685 presence of a very heterogeneous crust, *Geophysical Journal International*, **199**(1), 402–415.
- 686 Maraschini, M. & Foti, S., 2010. A Monte Carlo multimodal inversion of surface waves, *Geophysical Journal*  
687 *International*, **182**(3), 1557–1566.
- 688 Masini, E., Manatschal, G., Tugend, J., Mohn, G., & Flament, J. M., 2014. The tectono-sedimentary evolution  
689 of a hyper-extended rift basin: the example of the Arzacq-Mauléon rift system (Western Pyrenees, France),  
690 *Int. J. Earth Sci.*, **103**, 1569–1596.
- 691 Montagner, J. & Tanimoto, T., 1990. Global anisotropy in the upper mantle inferred from the regionalization



- 692 of phase velocities, *J. Geophys. Res.*, **95**, 4797–4819.
- 693 Mordret, A., Shapiro, N., Singh, S., Roux, P., & Barkved, O., 2013. Helmholtz tomography of ambient noise  
694 surface wave data to estimate Scholte wave phase velocity at Valhall Life of the Field, *GEOPHYSICS*, **78**(2),  
695 WA99–WA109.
- 696 Mordret, A., Landès, M., Shapiro, N. M., Singh, S. C., & Roux, P., 2014. Ambient noise surface wave to-  
697 mography to determine the shallow shear velocity structure at Valhall: depth inversion with a Neighbourhood  
698 Algorithm, *Geophysical Journal International*, **198**(3), 1514–1525, Publisher: Oxford Academic.
- 699 Mouthereau, F., Filleaudeau, P.-Y., Vacherat, A., Pik, R., Lacombe, O., Fellin, M. G., Castellort, S.,  
700 Christophoul, F., & Masini, E., 2014. Placing limits to shortening evolution in the pyrenees: Role of margin  
701 architecture and implications for the iberia/europe convergence, *Tectonics*, **33**(12), 2283–2314.
- 702 Olivet, J. L., 1996. La cinématique de la plaque ibérique, *Bull. Cent. Rech. Explor. Prod. Elf Aquitaine*, **20**(1),  
703 131–195.
- 704 Pedreira, D., Pulgar, J. A., Gallart, J., & Torné, M., 2007. Three-dimensional gravity and magnetic modeling  
705 of crustal indentation and wedging in the western Pyrenees-Cantabrian Mountains, *Journal of Geophysical  
706 Research*, **112**(B12).
- 707 Planès, T., Obermann, A., Antunes, V., & Lupi, M., 2019. Ambient-noise tomography of the Greater Geneva  
708 Basin in a geothermal exploration context, *Geophysical Journal International*, **220**(1), 370–383.
- 709 Podvin, P. & Lecomte, I., 1991. Finite difference computation of travel times in very contrasted velocity  
710 models: a massively parallel approach and its associated tools, *Geophysical Journal International*, **105**, 271–  
711 284.
- 712 Polychronopoulou, K., Lois, A., Martakis, N., Chevrot, S., Sylvander, M., Diaz, J., Villaseñor, A., Calassou,  
713 S., Collin, M., Masini, E., et al., 2018. Broadband, short-period or geophone nodes? quality assessment of  
714 passive seismic signals acquired during the maupasacq experiment, *First Break*, **36**(4), 71–76.
- 715 Puigdefàbregas, C. & Souquet, P., 1986. Tecto-sedimentary cycles and depositional sequences of the Mesozoic  
716 and Tertiary from the Pyrenees, *Tectonophysics*, **129**(1-4), 173–203.
- 717 Rat, P., 1988. The basque-cantabrian basin between the iberian and european plates some facts but still many  
718 problems, *Revista de la Sociedad geológica de España*, **1**(4), 327–348.
- 719 Razin, P., 1989. *Évolution tecto-sédimentaire alpine des Pyrénées basques à l'ouest de la transformante de*  
720 *Pamplona, Province du Labourd*, Ph.D. thesis, Bordeaux 3.
- 721 Richard, P., 1986. *Structure et évolution alpine des massifs paléozoïques du Labourd (Pays Basque français)*,  
722 Éditions du Bureau de recherches géologiques et minières.
- 723 Rosenbaum, G., Lister, G. S., & Duboz, C., 2002. Relative motions of Africa, Iberia and Europe during Alpine  
724 orogeny, *Tectonophysics*, **359**(1–2), 117–129.
- 725 Sambridge, M., 1999. Geophysical inversion with a neighbourhood algorithm—I. Searching a parameter  
726 space, *Geophysical Journal International*, **138**(2), 479–494, Publisher: Oxford Academic.
- 727 Saspiturry, N., 2019. *Évolution sédimentaire, structurale et thermique d'un rift hyper-aminci: de l'héritage*  
728 *post-hercynien à l'inversion alpine: exemple du bassin de Mauléon (Pyrénées)*, Ph.D. thesis, Bordeaux 3.

- 729 Saspiturry, N., Cochelin, B., Razin, P., Leleu, S., Lemirre, B., Bouscary, C., Issautier, B., Serrano, O., Lasseur,  
 730 E., Baudin, T., & Allanic, C., 2019a. Tectono-sedimentary evolution of a rift system controlled by Per-  
 731 mian post-orogenic extension and metamorphic core complex formation (Bidarray Basin and Ursuya dome,  
 732 Western Pyrenees), *Tectonophysics*, **768**, 228180.
- 733 Saspiturry, N., Razin, P., Baudin, T., Serrano, O., Issautier, B., Lasseur, E., Allanic, C., Thinson, I., & Leleu, S.,  
 734 2019b. Symmetry vs. asymmetry of a hyper-thinned rift: Example of the Mauléon Basin (Western Pyrenees,  
 735 France), *Marine and Petroleum Geology*, **104**, 86–105.
- 736 Saspiturry, N., Allanic, C., Razin, P., Issautier, B., Baudin, T., Lasseur, E., Serrano, O., & Leleu, S., 2020a.  
 737 Closure of a hyperextended system in an orogenic lithospheric pop-up, Western Pyrenees: The role of mantle  
 738 buttressing and rift structural inheritance, *Terra Nova*, **32**(4), 253–260.
- 739 Saspiturry, N., Lahfid, A., Baudin, T., Guillou-Frottier, L., Razin, P., Issautier, B., Le Bayon, B., Serrano,  
 740 O., Lagabrielle, Y., & Corre, B., 2020b. Paleogeothermal Gradients Across an Inverted Hyperextended Rift  
 741 System: Example of the Mauléon Fossil Rift (Western Pyrenees), *Tectonics*, **39**(10).
- 742 Schmandt, B. & Clayton, R. W., 2013. Analysis of teleseismic P waves with a 5200-station array in Long  
 743 Beach, California: Evidence for an abrupt boundary to Inner Borderland rifting, *J. Geophys. Res.*, **118**,  
 744 doi:10.1002/jgrb.50370, 1–19.
- 745 Schoeffler, J., 1982. Les transversales basco-landaises, *Bull. Cent. Rech. ELF-Aquitaine*, **6**, 257–263.
- 746 Shapiro, N. & Ritzwoller, M., 2002. Monte-carlo inversion for a global shear-velocity model of the crust and  
 747 upper mantle, *Geophysical Journal International*, **151**(1), 88–105.
- 748 Shapiro, N. M., Campillo, M., Stehly, L., & Ritzwoller, M. H., 2005. High-resolution surface-wave tomogra-  
 749 phy from ambient seismic noise, *Science*, **307**, 1615–1618.
- 750 Socco, L. V. & Boiero, D., 2008. Improved Monte Carlo inversion of surface wave data, *Geophysical Prospect-*  
 751 *ing*, **56**(3), 357–371.
- 752 Souriau, A. & Pauchet, H., 1998. A new synthesis of Pyrenean seismicity and its tectonic implications,  
 753 *Tectonophysics*, **290**, 221–244.
- 754 Tarantola, A. & Valette, B., 1982. Generalized nonlinear inverse problems solved using the least squares  
 755 criterion, *Reviews of Geophysics*, **20**(2), 219–232.
- 756 Teixell, A., Labaume, P., & Lagabrielle, Y., 2016. The crustal evolution of the west-central Pyrenees revisited:  
 757 Inferences from a new kinematic scenario, *Comptes Rendus Geoscience*, **348**(3-4), 257–267.
- 758 Teixell, A., Labaume, P., Ayarza, P., Espurt, N., de Saint Blanquat, M., & Lagabrielle, Y., 2018. Crustal struc-  
 759 ture and evolution of the pyrenean-cantabrian belt: A review and new interpretations from recent concepts  
 760 and data, *Tectonophysics*, **724**, 146–170.
- 761 Thomson, W. T., 1950. Transmission of Elastic Waves through a Stratified Solid Medium, *Journal of Applied*  
 762 *Physics*, **21**(2), 89–93, Publisher: American Institute of Physics.
- 763 Tryggvason, A., Rognvaldsson, S., & Flovenz, O., 2002. Three-dimensional imaging of the P-and S-wave  
 764 velocity structure and earthquake locations beneath Southwest Iceland, *Geophysical Journal International*,  
 765 **151**(3), 848–866.

- 766 Tugend, J., Manatschal, G., Kuszniir, N. J., Masini, E., Mohn, G., & Thinon, I., 2014. Formation and defor-  
767 mation of hyperextended rift systems: Insights from rift domain mapping in the Bay of Biscay-Pyrenees,  
768 *Tectonics*, **33**(7), 1239–1276.
- 769 Tugend, J., Manatschal, G., & Kuszniir, N., 2015. Spatial and temporal evolution of hyperextended rift systems:  
770 Implication for the nature, kinematics, and timing of the iberian-european plate boundary, *Geology*, **43**(1),  
771 15–18.
- 772 Vacher, P. & Souriau, A., 2001. A three-dimensional model of the Pyrenean deep structure based on gravity  
773 modelling, seismic images and petrological constraints, *Geophysical Journal International*, **145**(2), 460–470.
- 774 Van Hinsbergen, D. J., Torsvik, T. H., Schmid, S. M., Mañenco, L. C., Maffione, M., Vissers, R. L., Gürer, D.,  
775 & Spakman, W., 2020. Orogenic architecture of the mediterranean region and kinematic reconstruction of its  
776 tectonic evolution since the triassic, *Gondwana Research*, **81**, 79–229.
- 777 Vielzeuf, D. & Kornprobst, J., 1984. Crustal splitting and the emplacement of pyrenean lherzolites and gran-  
778 ulites, *Earth and Planetary Science Letters*, **67**(1), 87–96.
- 779 Villaseñor, A., Chevrot, S., Sylvander, M., Polychronopoulou, K., Martakis, N., Collin, M., Calassou, S., Díaz,  
780 J., Ruiz, M., Stehly, L., Boué, P., & Bitri, A., 2019. Crustal architecture of the Mauleon Basin (Western  
781 Pyrenees) from high resolution local earthquake tomography using the large-N Maupasacq experiment, in  
782 *Geophysical Research Abstracts*, vol. 21, EGU General Assembly.
- 783 Waldner, M., Bellahsen, N., Mouthereau, F., Bernet, M., Pik, R., Rosenberg, C. L., & Balvay, M., 2021.  
784 Central pyrenees mountain building: Constraints from new lt thermochronological data from the axial zone,  
785 *Tectonics*, **40**(3), e2020TC006614.
- 786 Wang, Y., Chevrot, S., Monteiller, V., Komatitsch, D., Mouthereau, F., Manatschal, G., Sylvander, S., Diaz,  
787 J., Ruiz, M., Grimaud, F., Benahmed, S., Pauchet, H., & Martin, R., 2016. The deep roots of the western  
788 Pyrenees revealed by full waveform inversion of teleseismic P waves, *Geology*, **44**(6), 475–478.
- 789 Xia, J., Miller, R., & Park, C., 1999. Estimation of near-surface shear-wave velocity by inversion of Rayleigh  
790 waves, *GEOPHYSICS*, **64**(3), 691–700.
- 791 Zhang, X., Curtis, A., Galetti, E., & de Ridder, S., 2018. 3-D Monte Carlo surface wave tomography, *Geo-*  
792 *physical Journal International*, **215**(3), 1644–1658.
- 793 Zolnai, G., 1975. Sur l'existence d'un réseau de failles de décrochement dans l'avant-pays nord des Pyrénées  
794 occidentales, *Rev Géogr Phys Géol Dynam Fr*, **17**, 219–238.

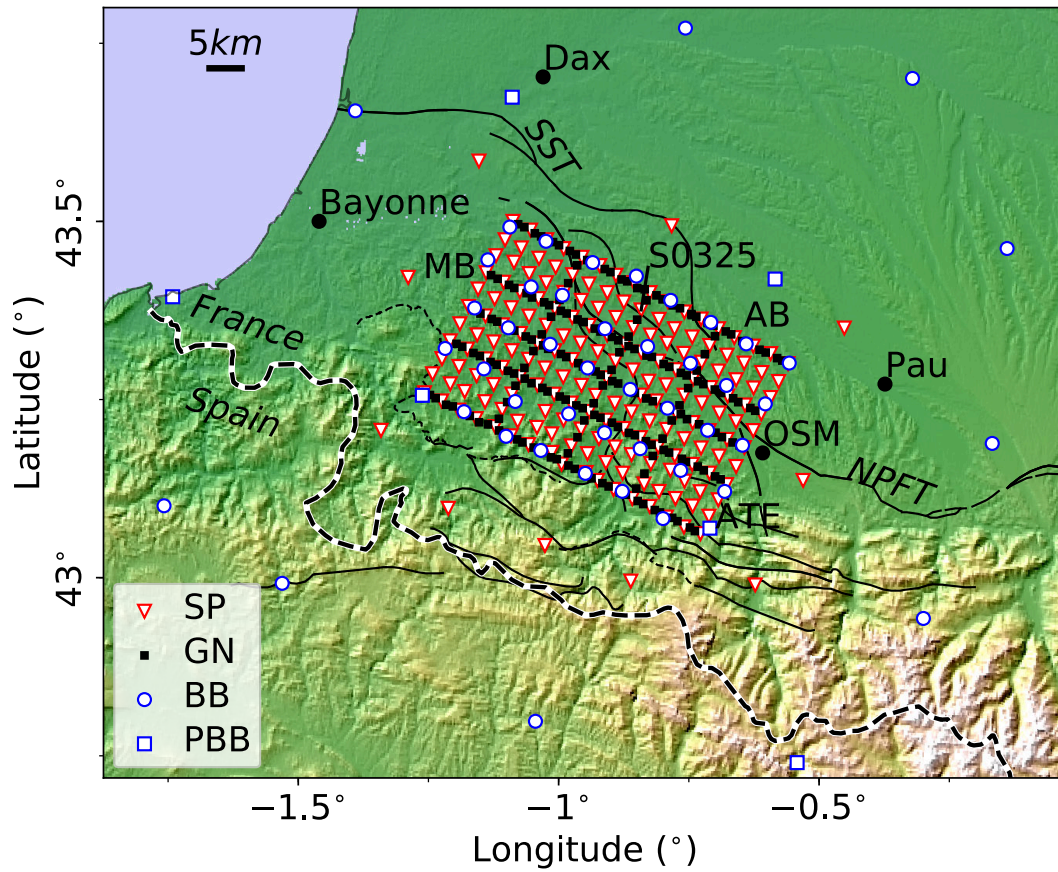


**Figure 1.** Map of stations (SP = short period, GN = Geophone nodes, BB = broadband, and PBB = permanent broadband) deployed during the Maupasacq experiment. OSM = Oloron-Sainte-Marie; AB = Arzacq Basin; MB = Mauléon Basin; NPFT = North Pyrenean Frontal Thrust; SST = Sainte-Suzanne Thrust. The solid lines indicate some of the known faults of the area, the thin dashed line SW of the survey indicates the contact between the Labourd Paleozoic basement and the sediments of the Mauléon basin and its equivalent along the Arbailles massif further to the south, see Fig. 2B. The thick dashed line delimits the French-Spanish border.

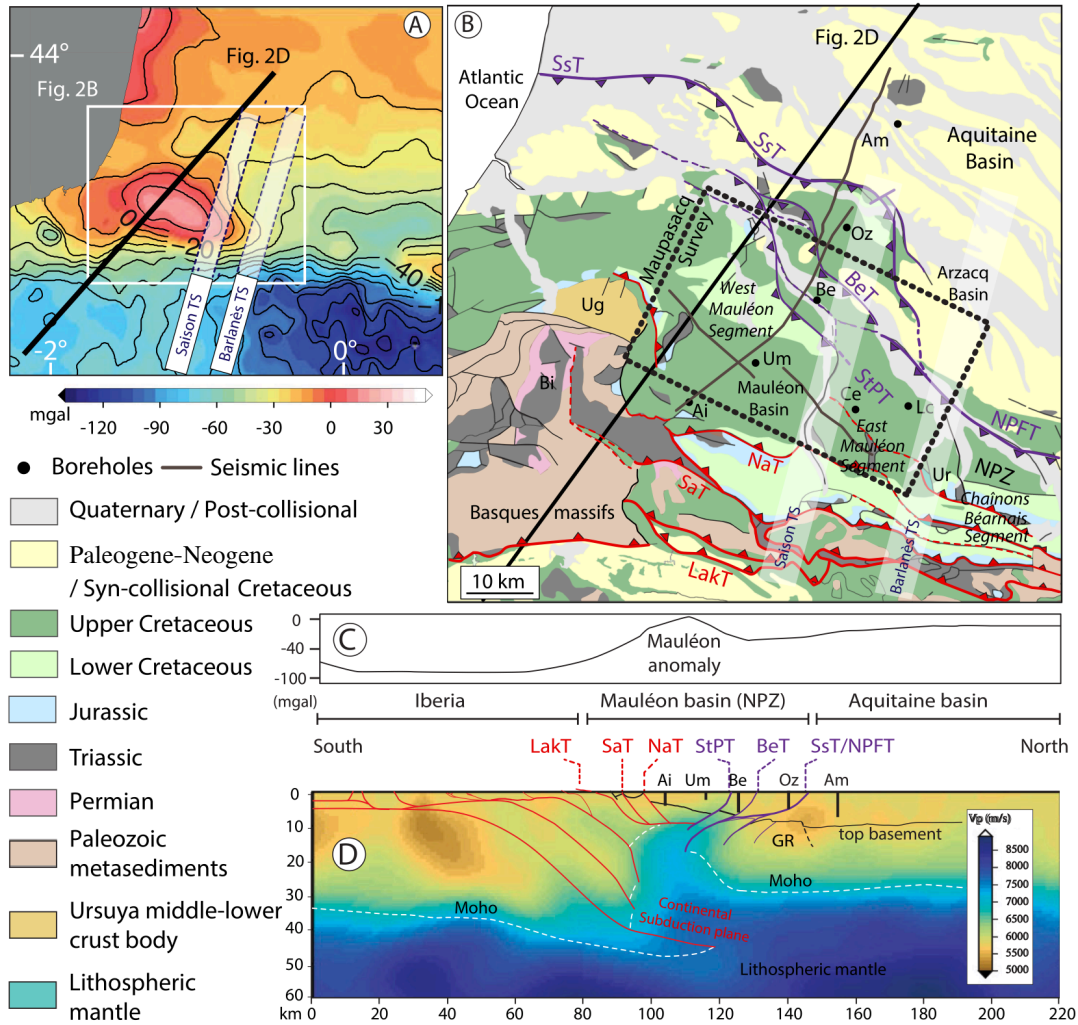


**Figure 2.**

**Figure 2.** Geological setting. (A) Bouguer gravity map of the western part of the Pyrenean belt (Casas et al. 1997), displaying a positive anomaly right upon the inverted hyperextended domain of the Mauléon basin. Dark line: location of the Wang et al. (2016) Vp model of subplot D. Contour intervals are 10 mgal. (B) Geological map illustrating the Mauléon basin pop-up structure (modified from Saspiturry 2019). Main south-vergent thrust faults underlined in red, match from north to south with the North Arbailles thrust (NaT), South Arbailles thrust (SaT), and the Lakhoura thrust (LakT). Main north-vergent thrust faults are represented in purple and correspond from south to north to the Saint-Palais thrust (St-PT), Bellevue thrust (BeT) and the Sainte-Suzanne thrust (SsT) representing the western termination of the North Pyrenean frontal thrust (NPFT). The white shaded bands oriented N20° indicate the Saison and Barlanès transverse structures (TS) discussed in the text. Seismic reflection profiles in dark grey have been used to calibrate the uppermost and northern part of the Saspiturry et al. (2020b) Mauléon basin section shown in subplot D. Ug—Ursuya granulites; Bi—Bidarray Permian Basin; Ur—Urdach mantle outcrop. Boreholes: Ai—Ainhice; Am—Amou; Be—Bellevue; Oz—Orthez; Um—Uhart-Mixe. Ce—Cheraute. Lc—Les Cassières. GR—Grand Rieu High. (C) Mauléon basin Bouguer anomaly profile (Casas et al. 1997). (D) P-wave crustal model by Wang et al. (2016) with superimposed interpretation by Saspiturry et al. (2020b).

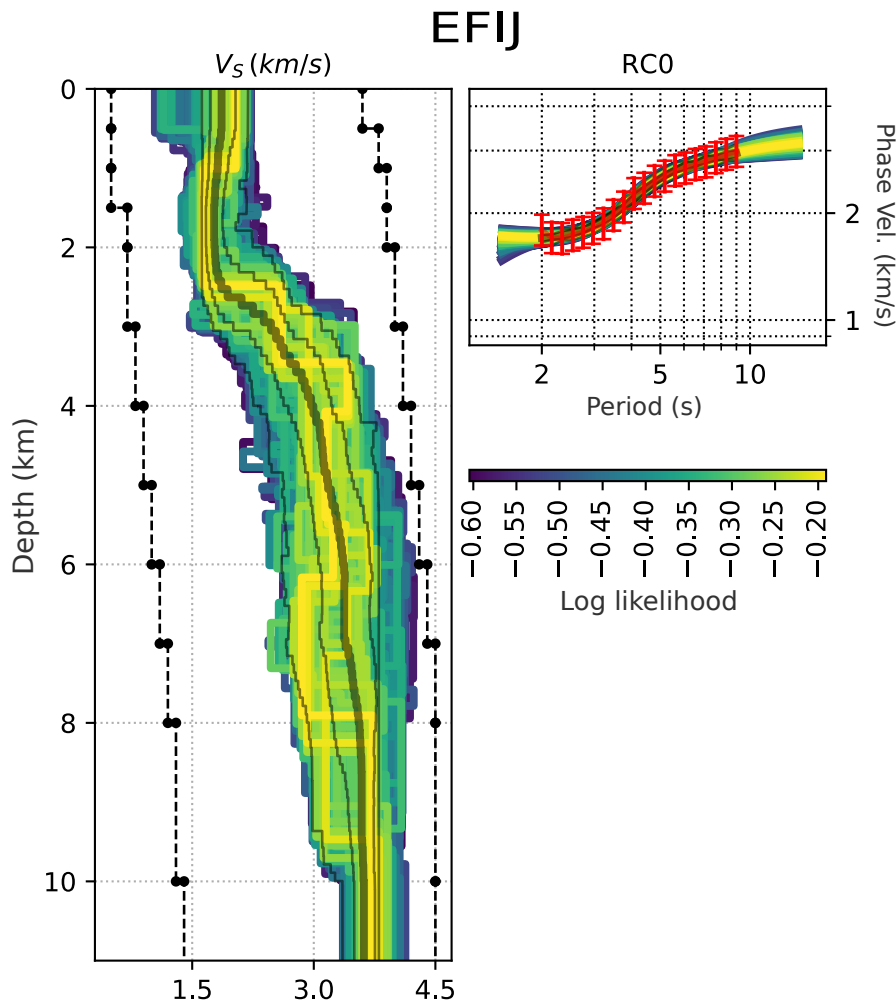


**Figure 3.** Result of the point-wise depth inversion for the grid point located at the intersection of slices EF and IJ as indicated in Figure 5. (Left panel) Model space : the dashed black lines indicate the boundaries of the search area. The colored  $V_S$  models indicate the best 1,000 models retained. The thick grey solid model indicates the median of the 1,000 best models found. (Right panel) Data space : the red curve with error bars indicates the observed Rayleigh wave phase velocity dispersion data to fit. The colored dispersion curves are the projection of the 1,000 best models onto the data space.

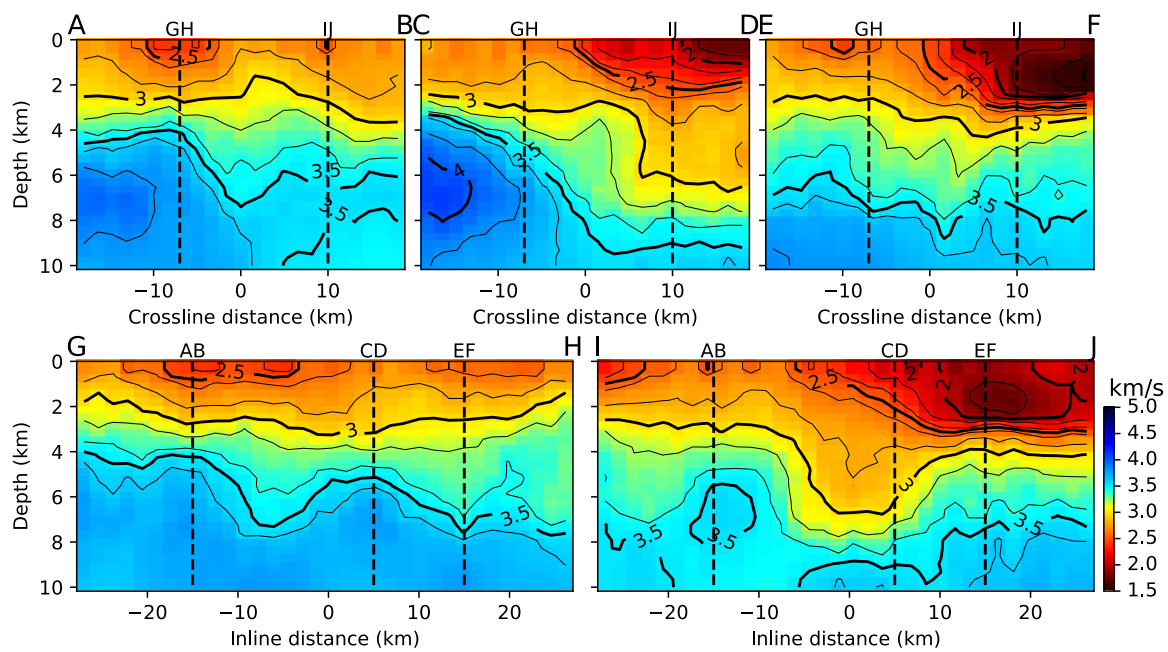


**Figure 4.** Vertical profiles across the prior  $V_S$  model obtained from point-wise depth inversion. The location of the slices are indicated in Figure 5.



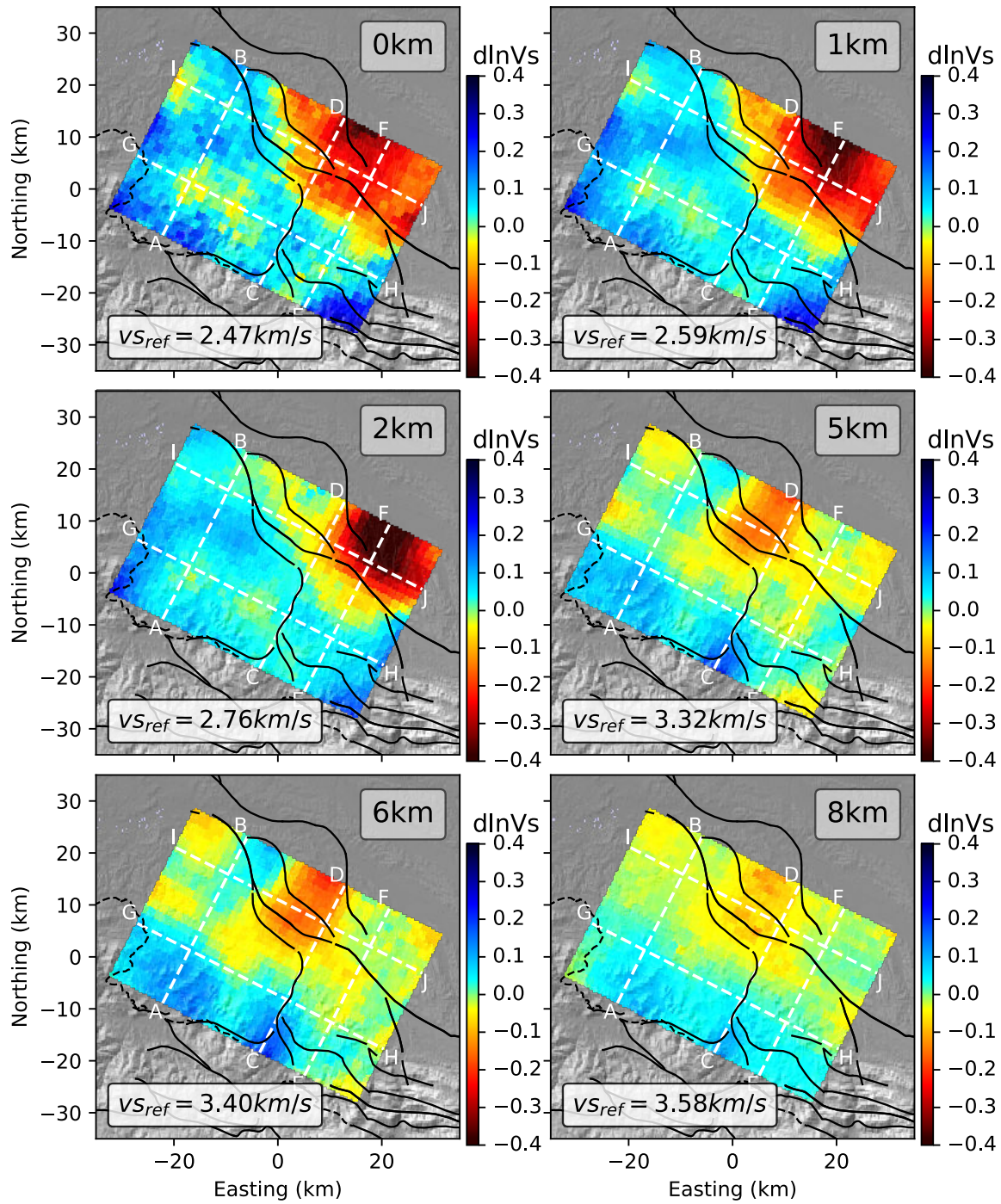


**Figure 5.** Horizontal sections across the prior  $V_S$  model obtained from point-wise depth inversion. The black lines indicate the surface location of the main faults after (Sasipiturry et al. 2019b).

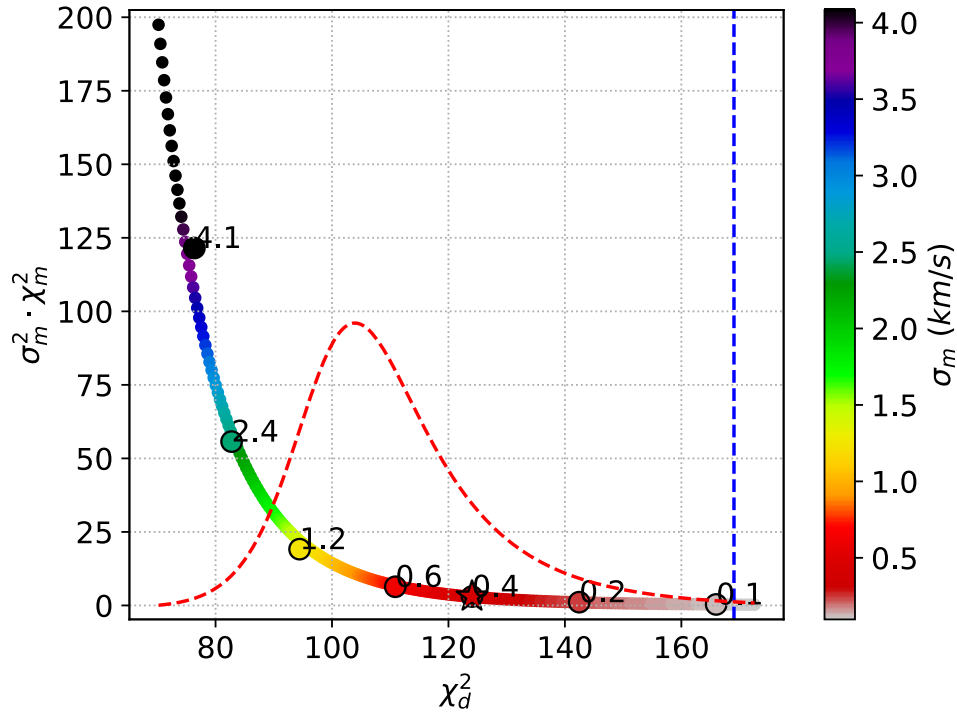


**Figure 6.** Regularization test. The colors indicate the value of the prior uncertainty used as a damping parameter ( $\sigma_m$ ). The red dashed curve is the curvature of the L-curve. The blue dashed line indicates the data cost of the prior model from point wise depth inversion.  $\chi_d^2$  indicates the data misfit term  $\frac{1}{2}[\mathbf{d}^{obs} - \mathbf{g}(\mathbf{m})]^T \cdot \mathbf{C}_d^{-1} \cdot [\mathbf{d}^{obs} - \mathbf{g}(\mathbf{m})]$  and  $\chi_m^2$  corresponds to the model norm  $\frac{1}{2}[\mathbf{m}_n - \mathbf{m}_0]^T \cdot \mathbf{C}_m^{-1} \cdot [\mathbf{m}_n - \mathbf{m}_0]$ .

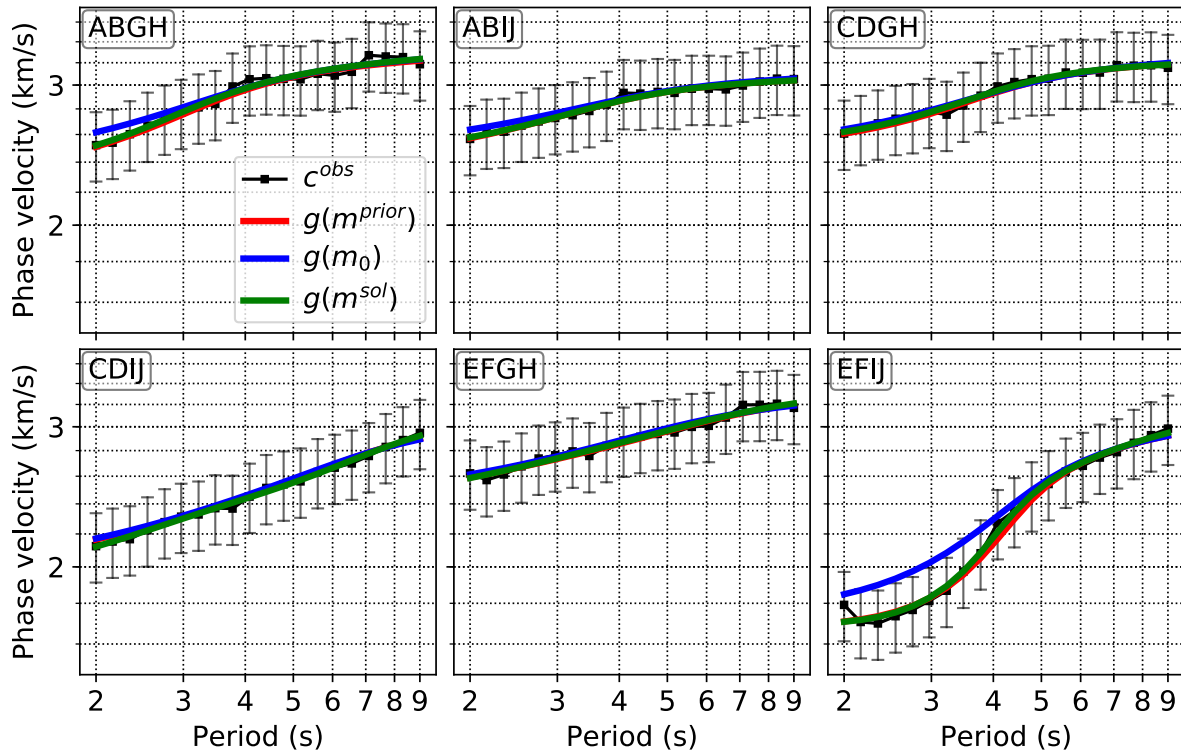


**Figure 7.** Observed and modeled Rayleigh wave phase velocity dispersion curves at the intersection between slices AB, CD, EF, GH and IJ (see Fig. 5).  $m^{prior}$ : model obtained from the point-wise inversion (step 1).  $m_0$ : smoothed version of the prior model, used to start the 3-D optimization (step 2);  $m^{sol}$ : solution of the 3-D optimization.

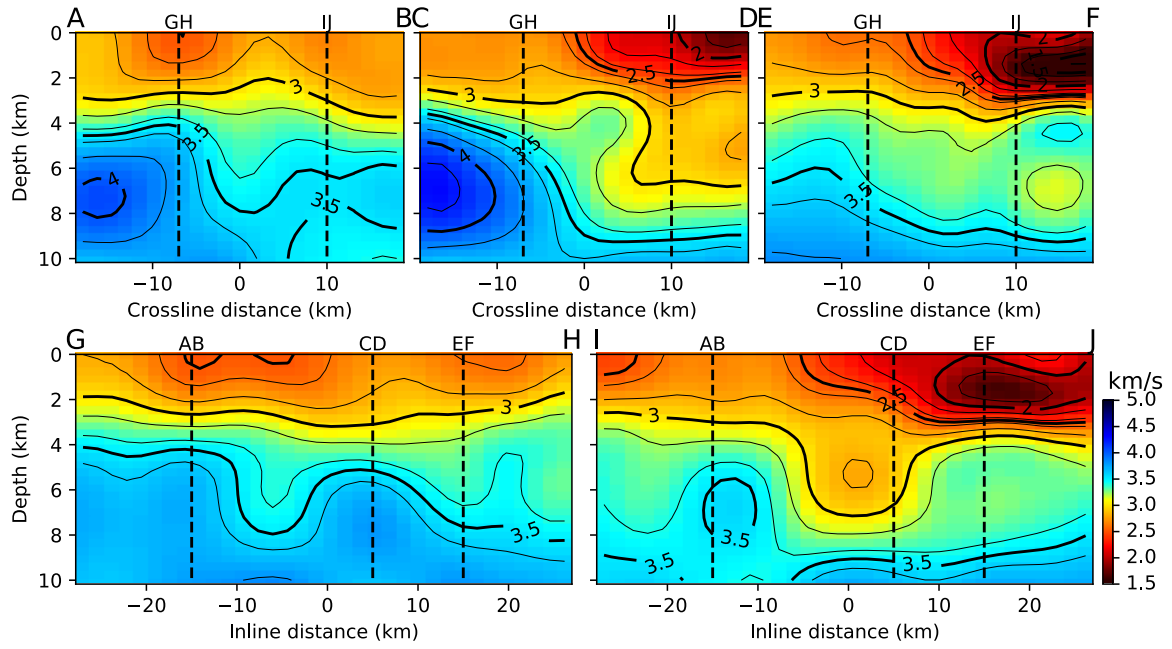


**Figure 8.** Vertical profiles across the final 3-D  $V_S$  model obtained from SWT. The location of the slices are indicated in Fig. 9

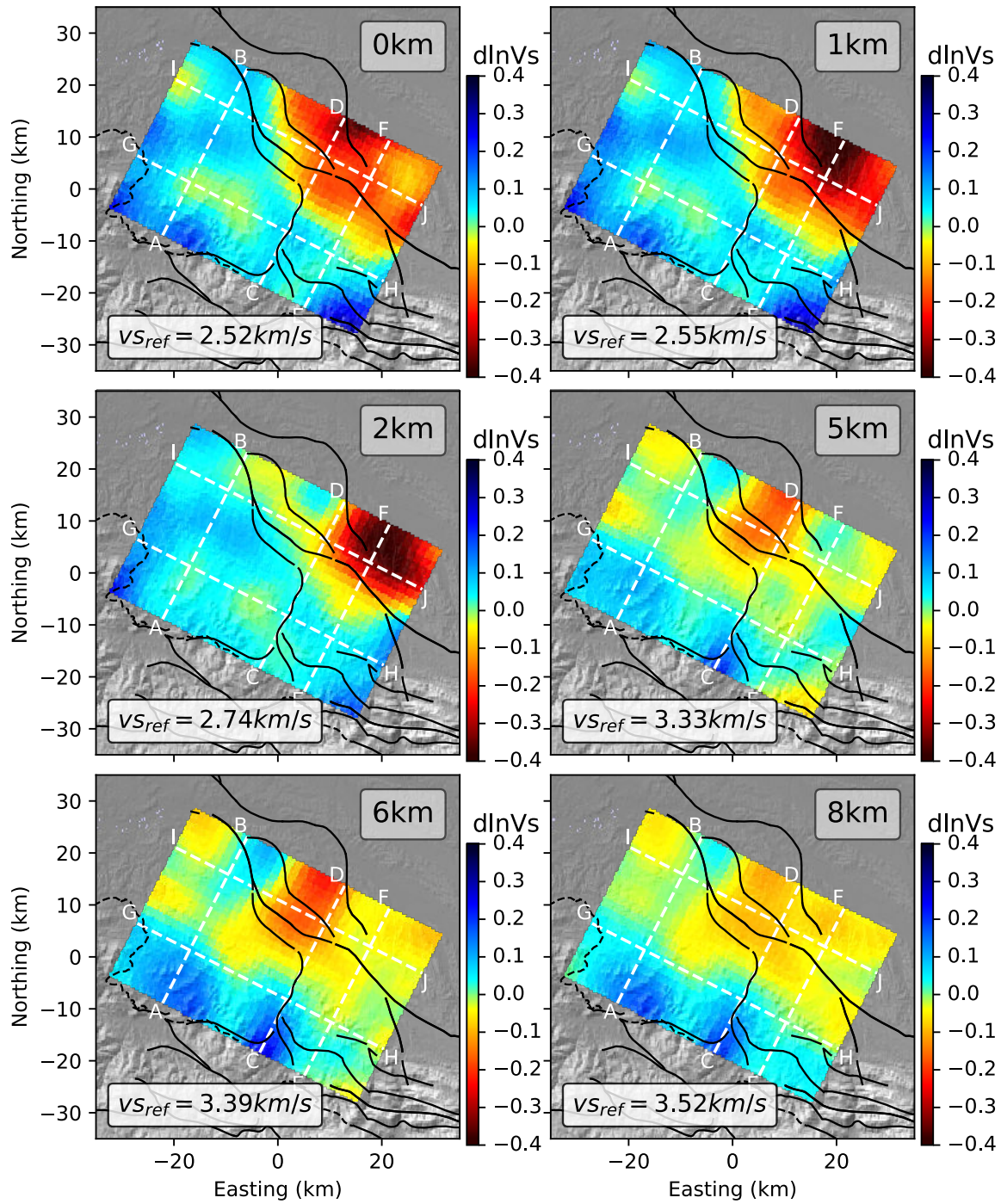


**Figure 9.** Horizontal sections in the final 3-D  $V_S$  model obtained from SWT. The black lines indicate the main faults.

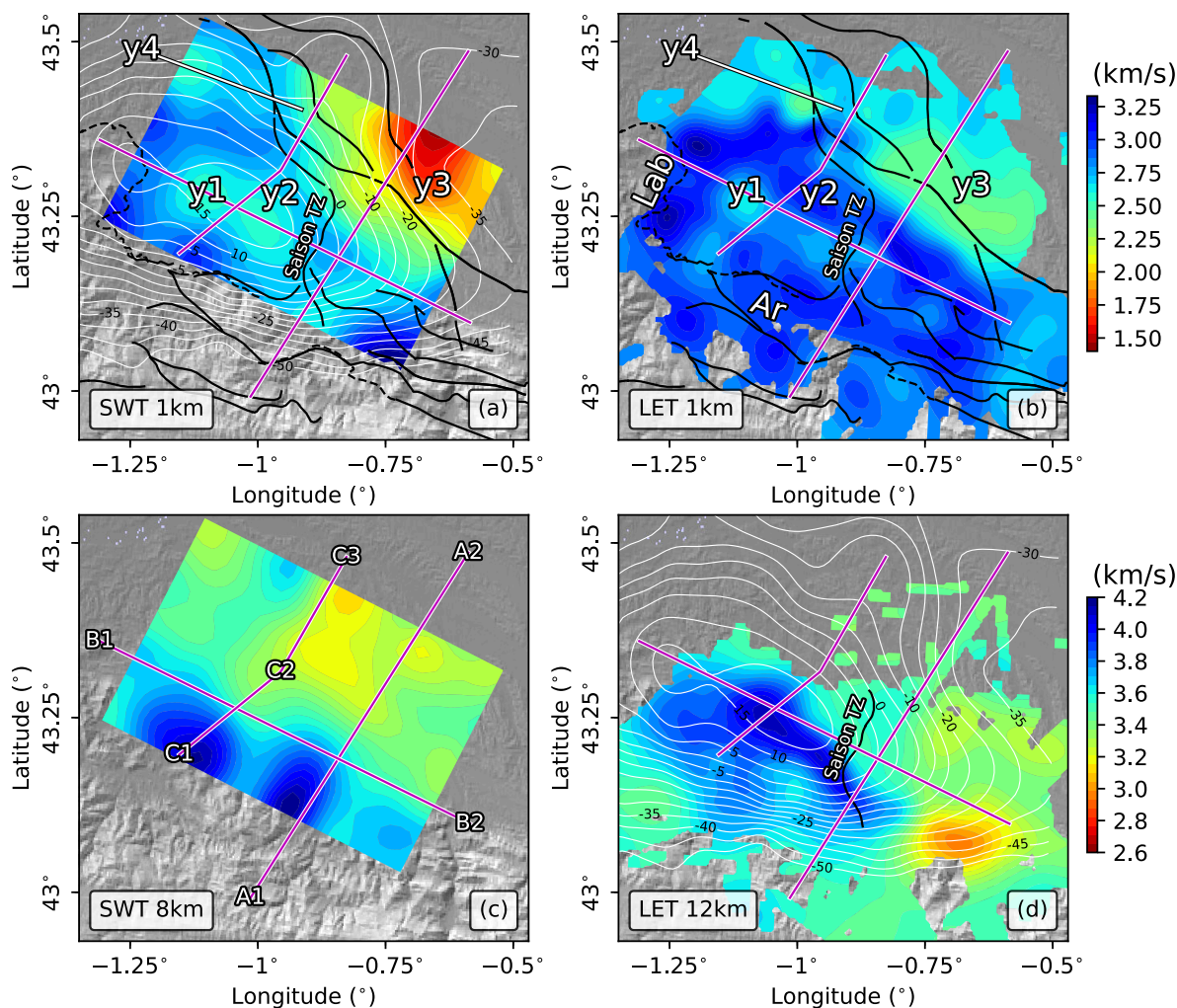


**Figure 10.** Map views of  $V_S$  models from SWT (a,c) and LET (b,d) at several depths. The pink lines indicate the positions of sections A1-A2, B1-B2, C1-C2-C3 shown in Figs. 11-16. The anomalies y1 to y4 are discussed in the text. The thick black lines correspond to main faults and the thin black dashed line corresponds to the basement-sediment interface to the south of the Mauléon basin. The thin white lines in maps (a, d) correspond to the contour of the Bouguer anomaly in mgal from Fig. 2A. Maps (a, b) and (c, d) share the same color bar. Ar: Arbailles massif; Lab: Labourd massif; Saison TS: Saison transverse structure.

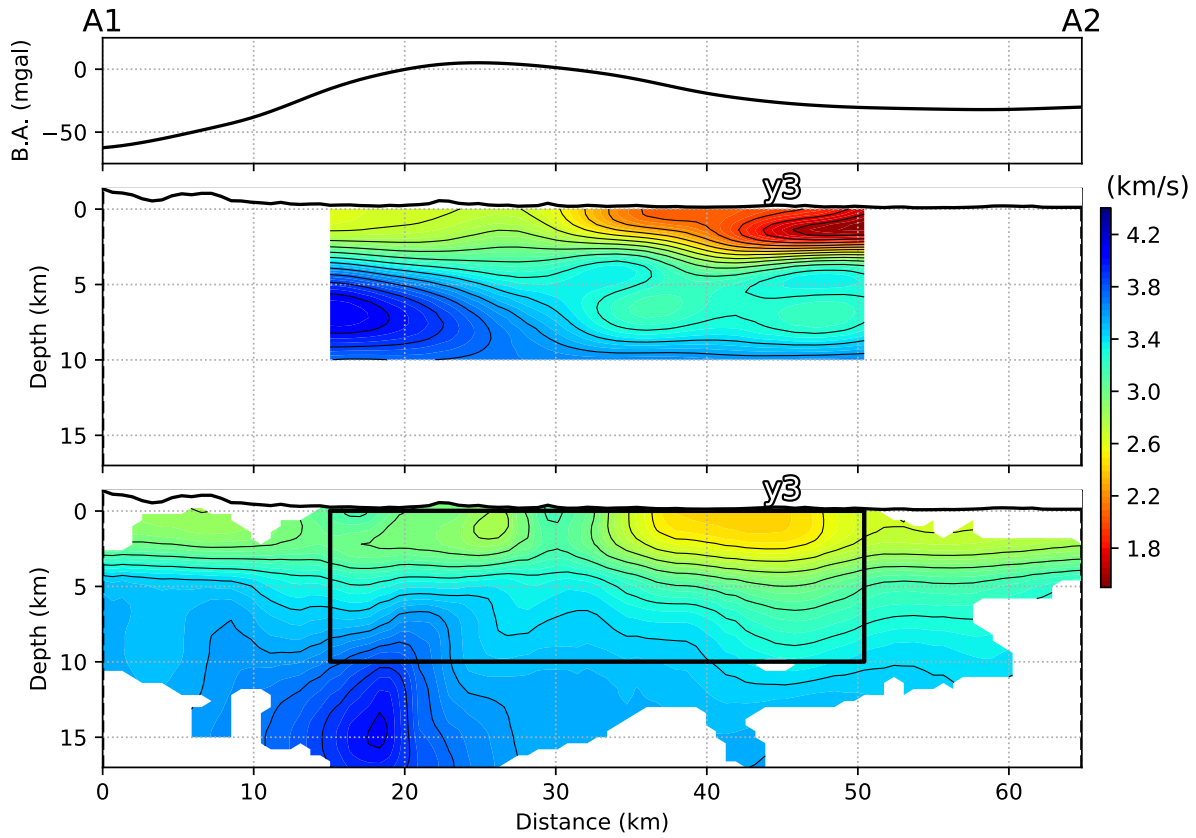


**Figure 11.** Comparison of Vs models obtained from SWT (top) and LET (bottom) along a SW-NE transect A1-A2 crossing the Arzacq basin (location in Fig. 10). Anomaly y3 is discussed in the text. B.A.: Bouguer Anomaly extracted along the profile from the gravity map of Fig. 2A.

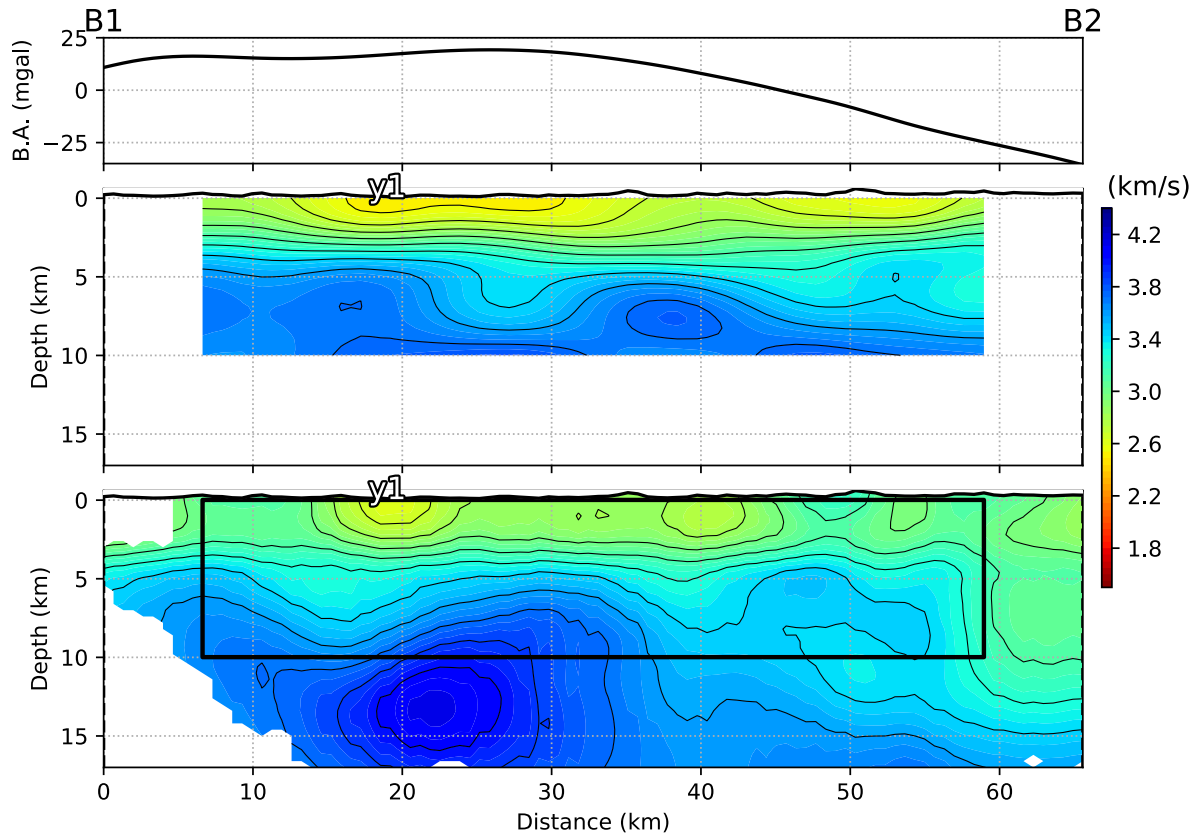


**Figure 12.** Comparison of Vs models obtained from SWT (top) and LET (bottom) along a WNW-ESE transect B1-B2 crossing the Mauléon basin (location in Fig. 10). Anomaly y1 is discussed in the text. B.A.: Bouguer Anomaly extracted along the profile from the gravity map of Fig. 2A.



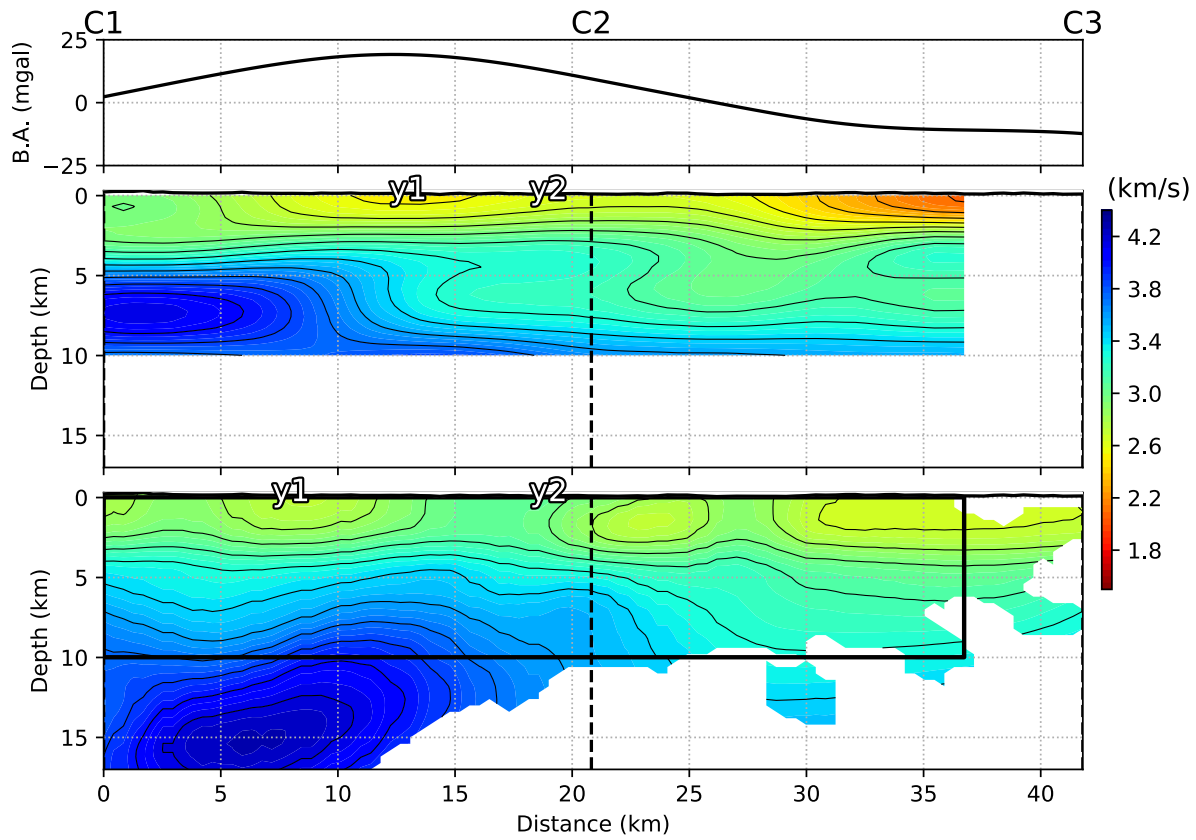


**Figure 13.** Comparison of  $V_s$  models obtained from SWT (top) and LET (bottom) along a SW-NE transect C1-C2-C3 crossing the Mauléon basin (location in Fig. 10). Anomalies  $y_1$ ,  $y_2$  are discussed in the text. B.A.: Bouguer Anomaly extracted along the profile from the gravity map of Fig. 2A.

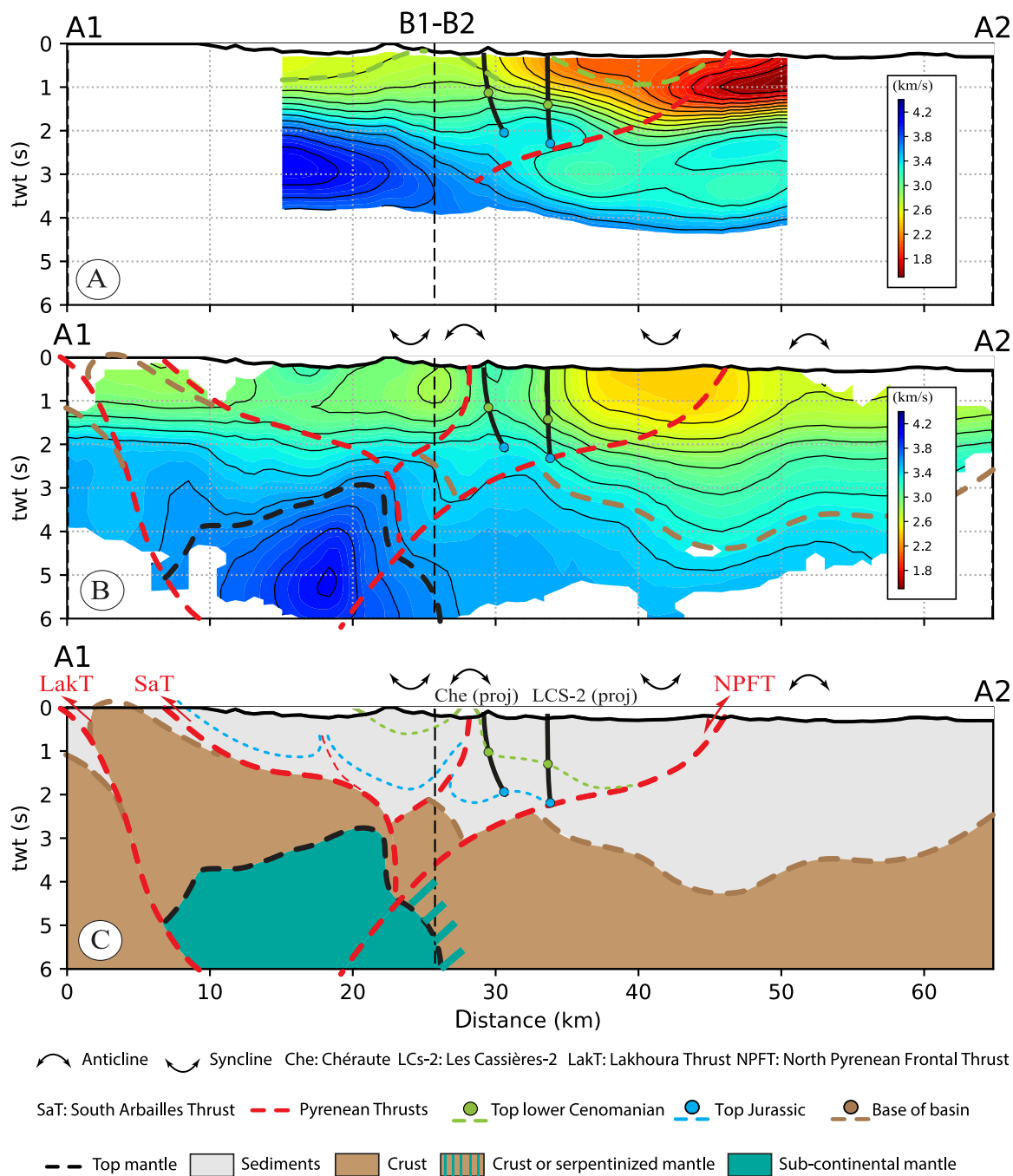


**Figure 14.** SW-NE profile in the eastern Mauléon basin showing the interpretation of the SWT (A) and LET (B) models. The final geological interpretation (C) is based on these models, the surface geology and boreholes. Location of axial traces of major anticlines and synclines are based on the geological map. The surface wave model successfully images the first-order basin architecture at shallow depth (syncline/anticline, faults) whereas the local earthquake tomography model provides information about the basement-sediment interface and the geometry of the high velocity body at depth.

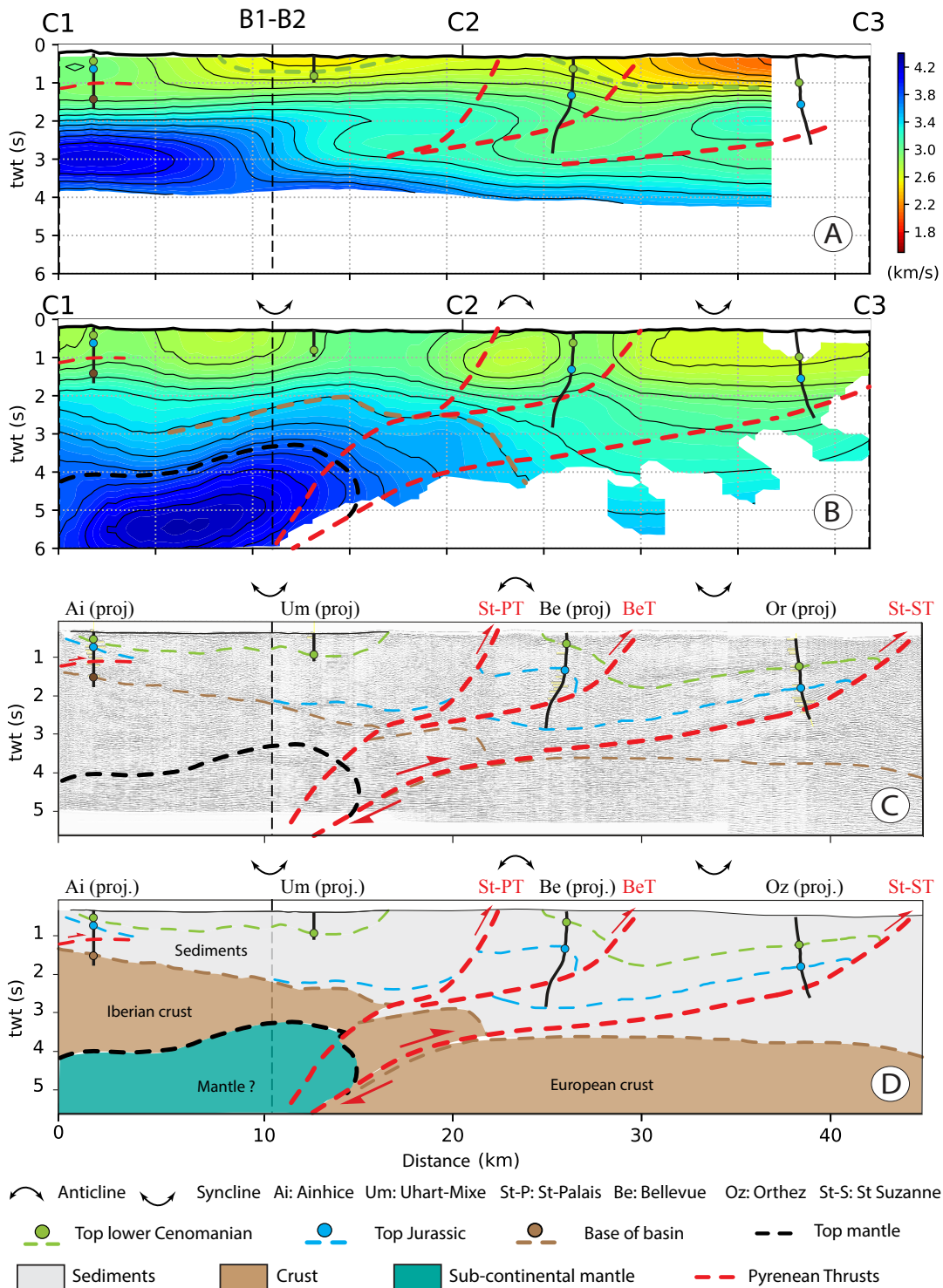


**Figure 15.** SW-NE profile in the western Mauléon basin showing the interpretation of the SWT model (A), the LET model (B), the NS seismic reflection profile (C) and the final geological interpretation (D). Note the difference in the basin architecture and the basement geometry in comparison to the eastern Mauléon section of Fig. 14.

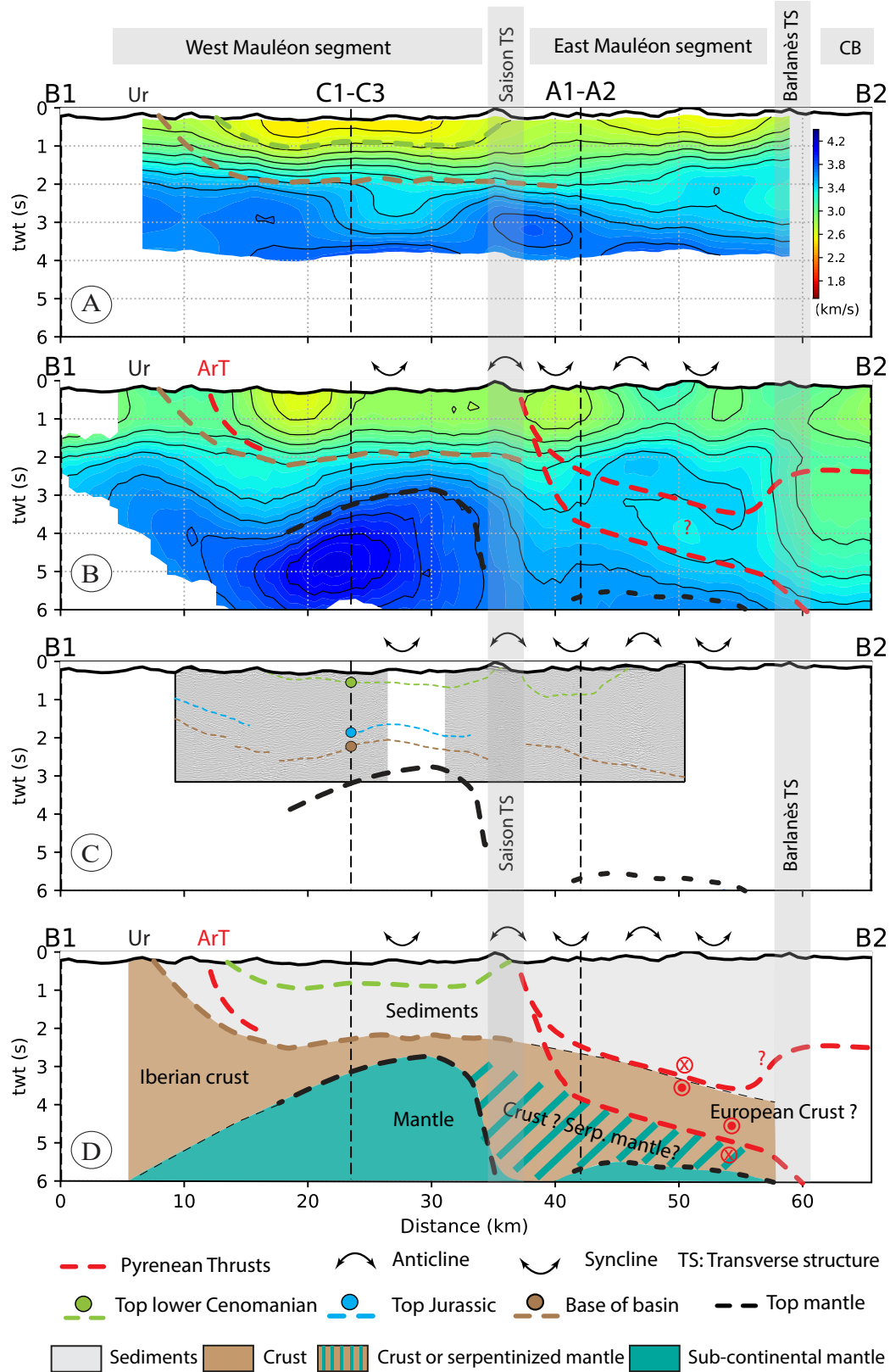
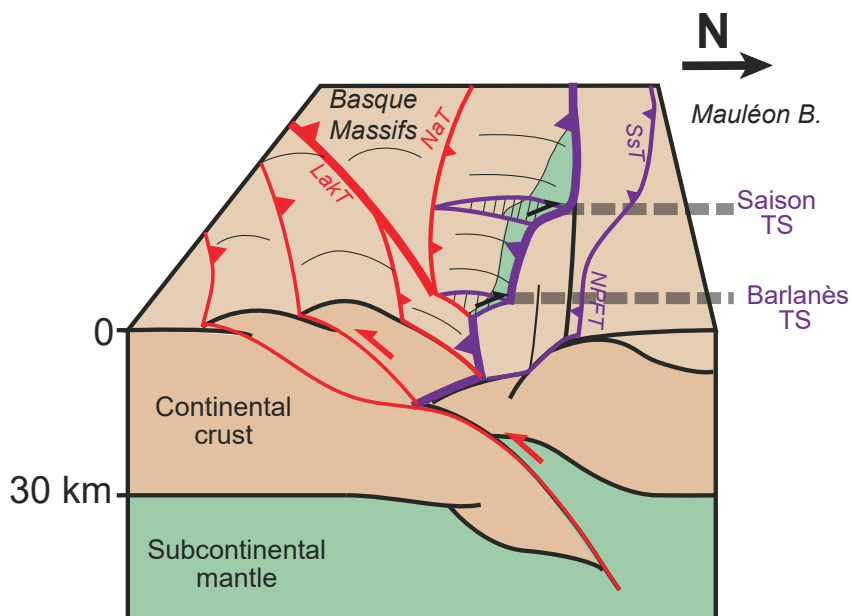


Figure 16.

**Figure 16.** WNW-ESE profile in the Mauléon basin showing the interpretation of the SWT model (A), the LET model (B), the seismic reflection profile (C) and the geological interpretation (D). Note the very high velocity body in the Western Mauléon segment of the section, contrasting with the complex velocity inversion in the Eastern Mauléon segment and the low velocity body in the Chaînons Béarnais segment, highlighting the importance of the Saison and Barlanès TS for the along-strike orogenic architecture of the study area. Correlating this section with the N-S sections further reveal that the intermediate unit bracketed by two velocity inversions in the Eastern Mauléon segment should be the tip of the European unit i.e. the European indenter between two thrusts.



**Figure 17.** Schematic 3-D block diagram showing the segmentation of the crustal architecture in the Mauléon basin as inferred from this study. Note the sampling of hyper-extended crust and mantle towards the west across the Saison and Barlanès TS. Basin sediments are not represented to highlight the basement structures. Annotations correspond to figure 2. Figure modified after Lescoutre & Manatschal (2020).

**Supplementary materials for "Three-dimensional shear  
velocity structure of the Mauléon and Arzacq basins  
(Western Pyrenees)"**

M. Lehujeur, S. Chevrot, A. Villaseñor, E. Masini, N. Saspiturry,

R. Lescoutre, M. Sylvander & the Maupasacq Working Group

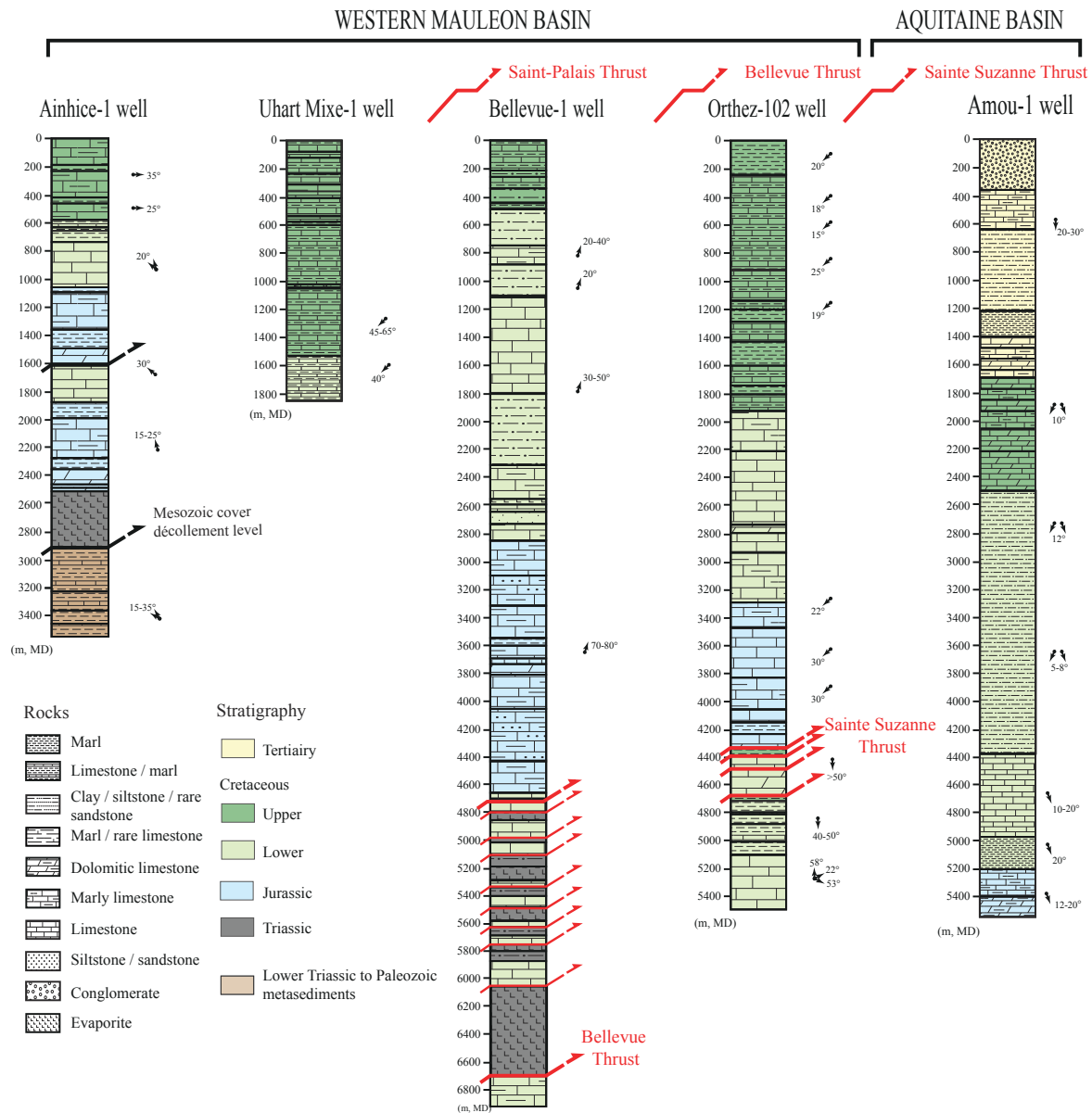


**Figure S1.** Wells data from the western segment covering the Mauléon basin in the south (Ainhice, Uhart-Mixe, Bellevue wells) and the Aquitaine basin (Amou well). Note that the intermediate Orthez well penetrates both the Mauléon and the Aquitaine basin units across the North-Pyrenean Frontal Thrust (NPFT). Note also that the Ainhice well reached the basement and that the Bellevue well drilled a vertical limb of a fold in its central part. After Saspiturry et al. (2019b, 2020b).

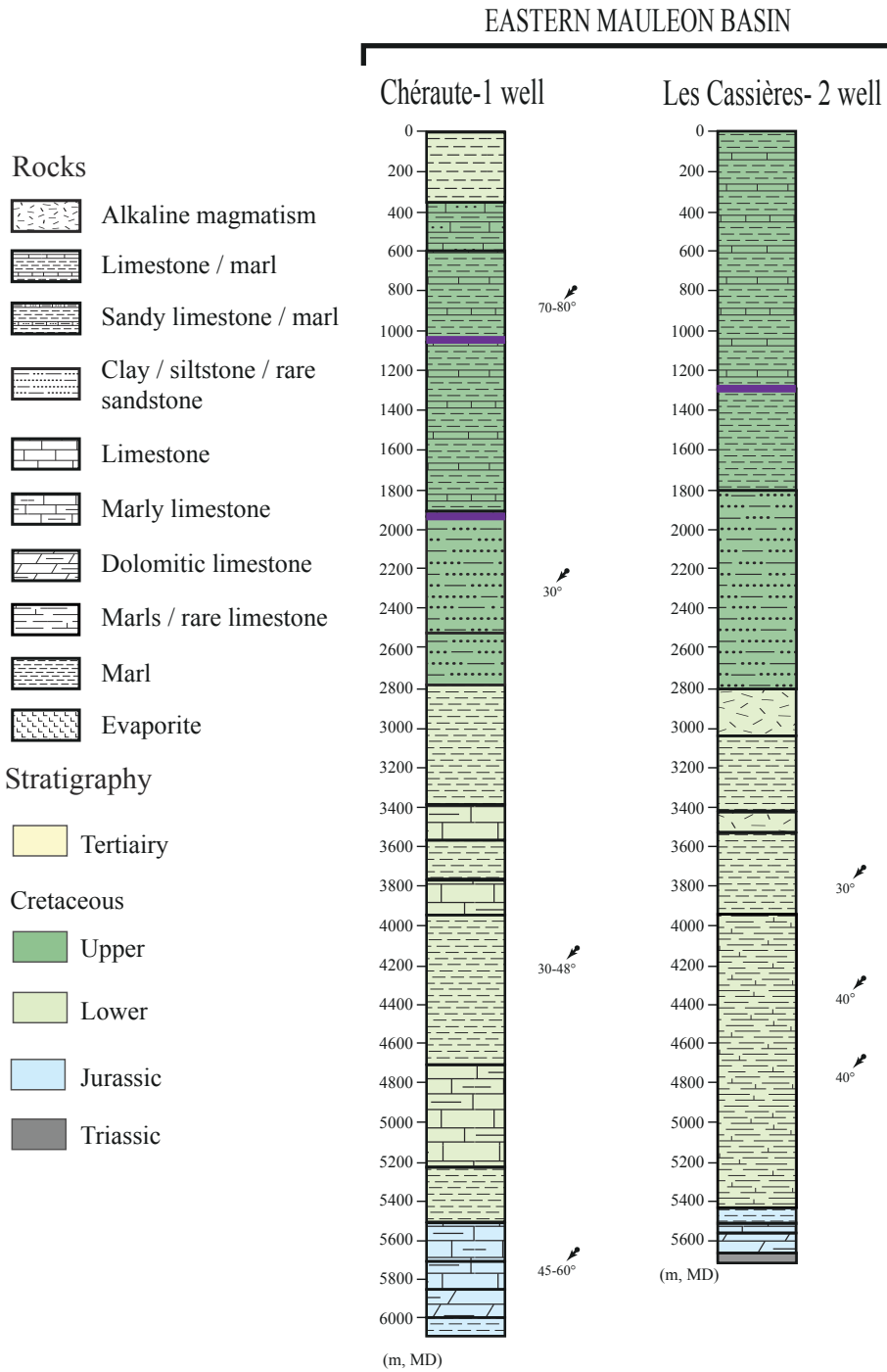


**Figure S2.** Wells data from the eastern segment covering the eastern Mauléon basin (Chéraute and Les Cassières-2 wells). After Saspiturry et al. (2019b, 2020b).



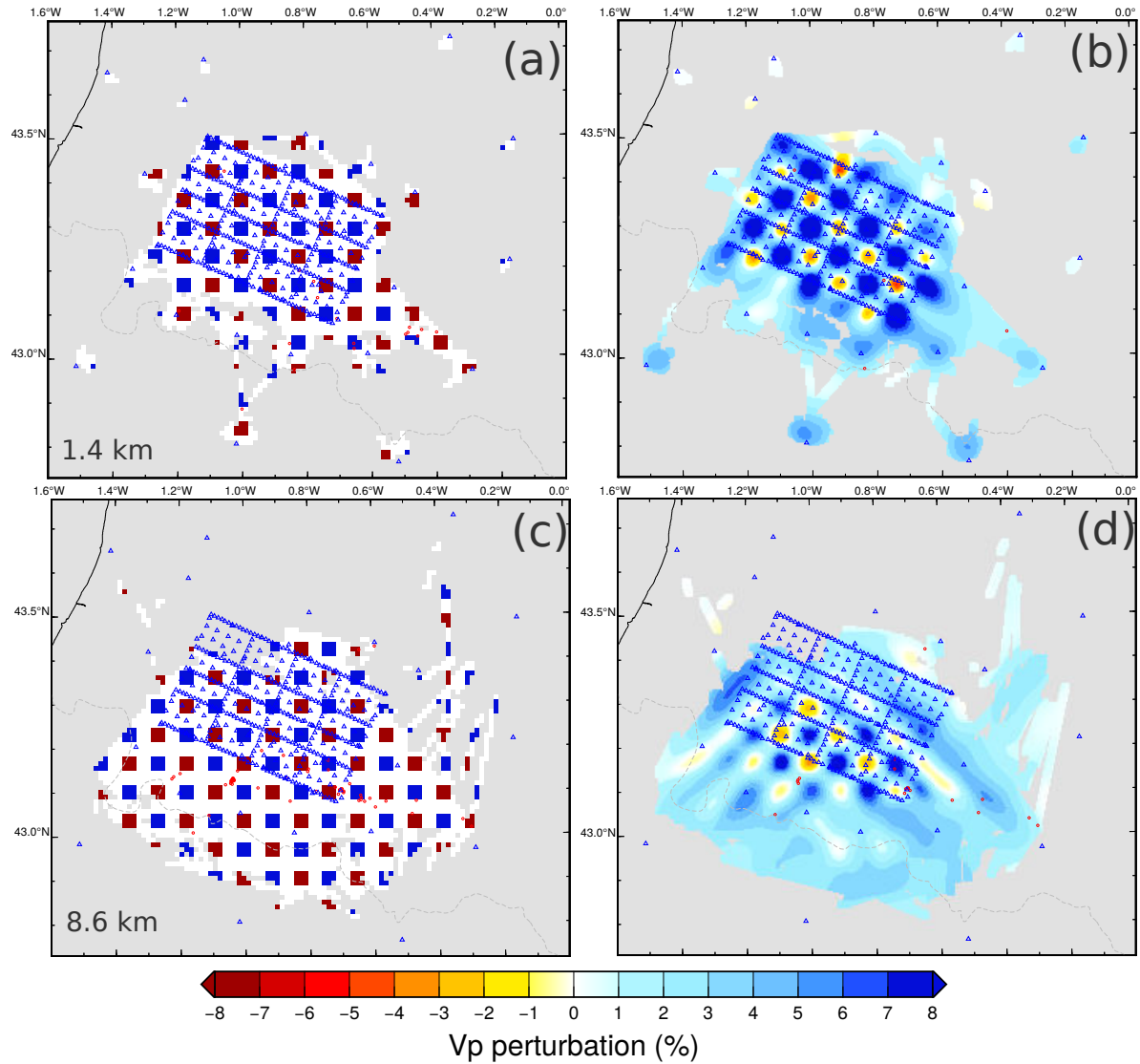


**Figure S3.** Checkerboard tests. (a) Synthetic checkerboard model at 1.4 km depth, including anomalies of  $\pm 10\%$  relative to the 1D model used for the starting model of the LET. The size of the checkers is  $3.6 \times 3.6 \times 3.6$  km. (b) result of the tomographic inversion at 1.4 km depth. (c, d) same as (a, b) at 8.6 km depth.